PNAS RESEARCH ARTICLE | CELL BIOLOGY

Galvanotactic directionality of cell groups depends on group size

Calina Copos[a,b,1], Yao-Hui Sun[c,d,1], Kan Zhu[c,d], Yan Zhang[e], Brian Reid[c,d], Bruce Draper[f], Francis Lin[g], Haicen Yue[h], Yelena Bernadskaya[i,j], Min Zhao[c,d,2], and Alex Mogilner[i,j,2]

Edited by David Weitz, Harvard University, Cambridge, MA; received August 14, 2024; accepted April 20, 2025

Motile cells migrate directionally in the electric field (EF) in a process known as galvanotaxis, an important phenomenon in wound healing and development. We previously reported that individual fish keratocyte cells migrate to the cathode in EFs, that inhibition of PI3 kinase (PI3K) reverses single cells to the anode, and that large cohesive groups of either unperturbed or PI3K-inhibited cells migrate to the cathode. Here, we report that small uninhibited cell groups move to the cathode, while small groups of PI3K-inhibited cells move to the anode. Small groups move faster than large groups, and groups of unperturbed cells move faster than PI3K-inhibited cell groups of comparable sizes. The shapes and sizes of large groups change little when they start migrating, while size and shapes of small groups change significantly, and lamellipodia disappear from the rear edges of these groups. The computational model, according to which cells inside and at the edge of the group interpret directional signals differently, explains the observations. Namely, cells in the group interior are directed to the cathode independently whether they are PI3K-inhibited or not. Meanwhile, the edge cells behave like individual cells: They are directed to the cathode in uninhibited groups and to the anode in PI3K-inhibited groups. As a result, all cells drive uninhibited groups to the cathode, while larger PI3K-inhibited groups are directed by cell majority in the group interior to the cathode, while majority of the edge cells in small groups win the tug-of-war driving these groups to the anode.

collective cell migration | galvanotaxis | PI3 Kinase

Significance

Motile cells migrate directionally in electric fields. This behavior—galvanotaxis—is important in many physiological phenomena. Individual fish keratocytes migrate to the cathode, while inhibition of PI3-Kinase (PI3K) reverses single cells to the anode. Uninhibited cell groups move to the cathode. Surprisingly, groups of PI3K-inhibited cells exhibit bidirectional behavior: Large groups move to the cathode, while small groups move to the anode. A mechanical model suggests that a tug-of-war between the outer and inner cells directs the cell groups.

Cells migrate collectively, as cohesive groups, in development, wound healing, and tumor invasion (1–3). Understanding the coordinated movement and directionality of these groups is an important open problem. Experimental research (1, 2, 4) on and modeling (5–8) of cell groups migrating spontaneously or in chemical gradients brought much insight into mechanics and directional cell behavior. A few conceptual models emerged from this research: A) Leader cells (9, 10) are polarized and actively migrating in the direction of an external cue. The remaining cells follow the leader cells passively (7). B) Inner cells in the group polarize in the direction of the external cue and migrate actively, while cells at the group edge do not respond to the directional signal and are dragged and pushed along by the inner cells (8, 11). C) The group is integrated mechanically (12, 13), so that all cells are tightly interlinked into a supracellular tissue by cytoskeletal structures spanning the whole group (14), and the groups migrate like one giant cell. More complex and nuanced models have also been considered (15, 16).

Much research on collective cell migration was done on groups moving in chemical gradients, yet there are other directional cues that cells encounter. Cells are electrical units: They transport ions across membranes and as a result are surrounded and regulated by electrical fields and currents (3, 12). The ability of cells to sense the direction of an electric field (EF)—galvanotaxis—plays important roles in development (17), wound healing (18), and regeneration (19). Some types of cells (i.e., keratinocytes) individually migrate to the cathode (positively charged terminal) in EF, others (i.e., fibroblasts)—to the anode (negatively charged terminal) (20). Respective galvanotactic signals may be as potent as, or even more important than, chemotactic signals (21). Electrically sensitive cells is the rule, not the exception (21). Most of research on the galvanotaxis was done on single cells, but recent studies also investigate collective migration in EF of epithelial cell sheets (22, 23), Madin-Darby canine kidney cell groups and keratinocytes (11, 24), corneal epithelial cells (25), and HaCaT cellular monolayers (26).

One cell type, fish epidermal keratocyte, has been instrumental in studying mechanisms of galvanotaxis due to its fast and steady locomotion, simple shape, and well-understood motile mechanics (27). Keratocytes sense EF and move to the cathode (28). Physically, keratocytes likely sense EF by harnessing electrophoresis of charged mobile transmembrane proteins, which aggregate to one of the cell's sides in EF (29) and serve either as receptors activating intracellular signaling relays, or as scaffolds for such receptors. Inhibition of

Author affiliations: [a]Department of Biology, Northeastern University, Boston, MA 02115; [b]Department of Mathematics, Northeastern University, Boston, MA 02115; [c]Department of Ophthalmology and Vision Science, School of Medicine, University of California, Davis, Sacramento, CA 95817; [d]Department of Dermatology, School of Medicine, University of California, Davis, Sacramento, CA 95817; [e]Department of Occupational and Environmental Health, Hangzhou Normal University School of Public Health, Hangzhou 311121, China; [f]Department of Molecular and Cellular Biology, University of California, Davis, Davis, CA 95616; [g]Department of Physics and Astronomy, University of Manitoba, Winnipeg, MB R3T 2N2, Canada; [h]Department of Physics, University of Vermont, Burlington, VT 05405; [i]Courant Institute, New York University, New York, NY 10012; and [j]Department of Biology, New York University, New York, NY 10012

Author contributions: C.C., Y.-H.S., M.Z., and A.M. designed research; C.C. and Y.-H.S. performed research; K.Z., Y.Z., B.R., B.D., F.L., and H.Y. contributed new reagents/analytic tools; C.C., Y.-H.S., Y.B., M.Z., and A.M. analyzed data; and C.C., Y.-H.S., Y.B., and A.M. wrote the paper.

The authors declare no competing interest.

This article is a PNAS Direct Submission.

[1]C.C. and Y.-H.S. contributed equally to this work.

[2]To whom correspondence may be addressed. Email: minzhao@ucdavis.edu or mogilner@cims.nyu.edu.

This article contains supporting information online at https://www.pnas.org/lookup/suppl/doi:10.1073/pnas.2416440122/-/DCSupplemental.

Published May 20, 2025.

PI3-Kinase (PI3K, for brevity) redirects these cells to the anode (29, 30). Both single keratocyte migration, and spontaneous migration of groups of zebrafish (31) and gold fish (5) keratocytes, as well as EF-induced collective movements of zebrafish (32, 33) and gold fish (28) keratocytes have been characterized.

PI3K is one of the key signaling molecules in pathways transducing the electrical signal to the cell motility apparatus (34), and individual PI3K-inhibited cells migrate to the anode (positive electric terminal), with large lamellipodia leading the way (30), oppositely to unperturbed individual cell migrating to the cathode (negative terminal). In (33), we reported that very large zebrafish keratocyte groups of thousands of uninhibited or PI3K-inhibited cells migrate to the cathode. To understand why individual PI3K-inhibited cells migrate to the anode but large groups of such cells—to the cathode, in this study, we use groups of several to tens to hundreds of cells to investigate their polarization, migration, and directional sensing in EF. We find that while larger (hundreds of PI3K-inhibited cells) groups move to the cathode and small (tens of PI3K-inhibited cells) groups move to the anode. These behaviors can be explained by a model according to which cells at the group edge sense EF in a similar way to the individual cells and tend to go to the cathode or anode depending on their unperturbed vs. PI3K-inhibited state. Meanwhile, cells in the group's interior are not passive followers, but rather tend to polarize and move to the cathode, independently of the state of PI3K signaling. In unperturbed groups, both inner and outer cells are driven to the cathode, and the whole group moves to the cathode. A tug-of-war between the inner and outer cells in PI3K-inhibited groups determines the group's directionality: In larger groups, the inner cell majority drives the group to the cathode; in small groups, the outer cell majority drives the group to the anode.

Results

Collective Behavior of Two Cohesive Cells Suggests Directional/Mechanical Rules for Outer Cells. To understand directionality of a cohesive pair of cells in EF, we observed such PI3K-inhibited pair (Fig. 1*A*) and saw that before EF was on, each of the two cells resembled a half-disc, with shared segment of a boundary and semicircular protruding lamellipodium. Straightforward interpretation of this morphology is that the common cohesive rear of this pair does not protrude due to the contact inhibition of locomotion (35) and that as far as this common rear position is determined by the cohesive intercellular contact, both cells become strongly polarized outward due to the ubiquitous tendency of motile cells to generate oppositely oriented contractile rear and protrusive front (36, 37). The clear indication of the propulsive force trying to move each cell away from the shared rear is that sometimes the cohesion in the central parts of the rear ruptures, and the cells' rears, held together just by two contacts at the sides, curve outward pulled by respective protrusions (frame 2 of Fig. 1*A*). When the EF is on (blue-bracketed frames of Fig. 1*A*), initially the cells stay cohesive, but, notably, start shifting together slowly in the anode direction (Movie S1 and compare two first blue-bracketed frames of Fig. 1*A*). This can be interpreted as the anode-facing lamellipodium of one of the cells being propelled by a stronger force than the oppositely cathode-facing lamellipodium of another cell, suggesting that there is a superposition of two types of forces. One is a constant-amplitude outward force trying to propel the cell in the direction normal to its rear, orientation of which is geometrically imposed by the contact with inner cells in the group, and another, EF-induced, directed along the anode–cathode axis, with amplitude graded by the angle between the anode (or cathode) and angle between this axis and the geometrically constrained rear–front axis of the lamellipodium. We use this concept to build the model of cell group collective directionality below.

After a few minutes of the tug-of-war between the two cells, they break contact, the initially cathode-facing cell makes a pivot to the anode and becomes a follower cell moving behind, and in touch with, the leader (last four frames of Fig. 1*A*). This hints at the phenomenon described below: When the group starts following the "correct," EF-informed, direction, the lamellipodia at the group's rear can destabilize, and the group's rear is made of rears of outer cells on that side.

Directionality of EF-Guided Cells and Cell Groups Depends on the State pf PI3K Signaling and Group Size. To confirm that the two-cell example is not an exception and that small groups of PI3K-inhibited cells move to the anode, we investigated keratocyte groups moving in physiological-range EF of magnitude 1 V/cm (38) (*Methods* and *SI Appendix*, Fig. S1) and recorded 30-min long trajectories of single cells and groups of various sizes (Fig. 1 *B*–*E*). We found that keratocyte groups of all sizes, in both control and PI3K-inhibited cases, did not respond directionally to weak EF of magnitude 0.5 V/cm, but became galvanotactic in EF of magnitude equal or greater than 1 V/cm (*SI Appendix*, Fig. S1); the directional response above the threshold was not sensitive to the EF strength. In the case of unperturbed cells, both single cells and groups of all sizes migrated to the cathode (Fig. 1 *B* and *C*). In the case of PI3K-inhibited cells, while large (more than 35 cells) groups also migrated to the cathode, majority of single cells and small (less than 35 cells) groups migrated oppositely, to the anode (Fig. 1 *D* and *E* and *SI Appendix*, Fig. S2). Statistics of the directedness—cosine of the angle between the vector connecting the initial and final positions of the groups' centroids and the cathode direction—confirm this result quantitatively (Fig. 1*F*); the anodal bias for the PI3K-inhibited groups increases with the degree of the PI3K inhibition (*SI Appendix*, Fig. S3). We also measured trajectory speed of the cells and groups (Fig. 1*G*) and found that individual cells, both unperturbed and PI3K-inhibited, moved faster than respective groups, and that the small groups, despite large variations of the speed between the groups, moved faster than the large groups (Fig. 1*G*; small and large unperturbed groups moved with speeds ≈4.07 μm/min and ≈3.34 μm/min, respectively, while small and large PI3K-inhibited groups moved with speeds ≈3.94 μm/min and ≈3.35 μm/min, respectively).

One-Dimensional (1D) Mechanical Model of the Tug-of-War between the Outer and Inner Cells Explains the Size-Dependent Group Directionality. Quantitative modeling has been instrumental in understanding collective cell directionality in chemical gradients (7, 39, 40) and individual cell directionality in EF (41, 42). Individual (43–46) and collective (13, 43, 47) cell mechanics have also been modeled, and altogether these theories suggest the following simple conceptual model that helps to begin understanding the bidirectional group motility in EF (Fig. 1*H*). Let us consider a 1D cohesive chain of cells stretching from the anodal to cathodal edge of the group (Fig. 1*H*), and for now, consider this cell chain in isolation, without contacts with other cells on the sides. Based on measurements of responses of the cells to EF within very large groups (33), we will assume that all cells in the chain, including the inner and outer (edge) cells, sense EF and respond to it individually and independently. Following previous modeling work, we will also assume that each cell in the chain responds to EF by generating a propulsion force, direction, and magnitude which depends on the cell position within the group.

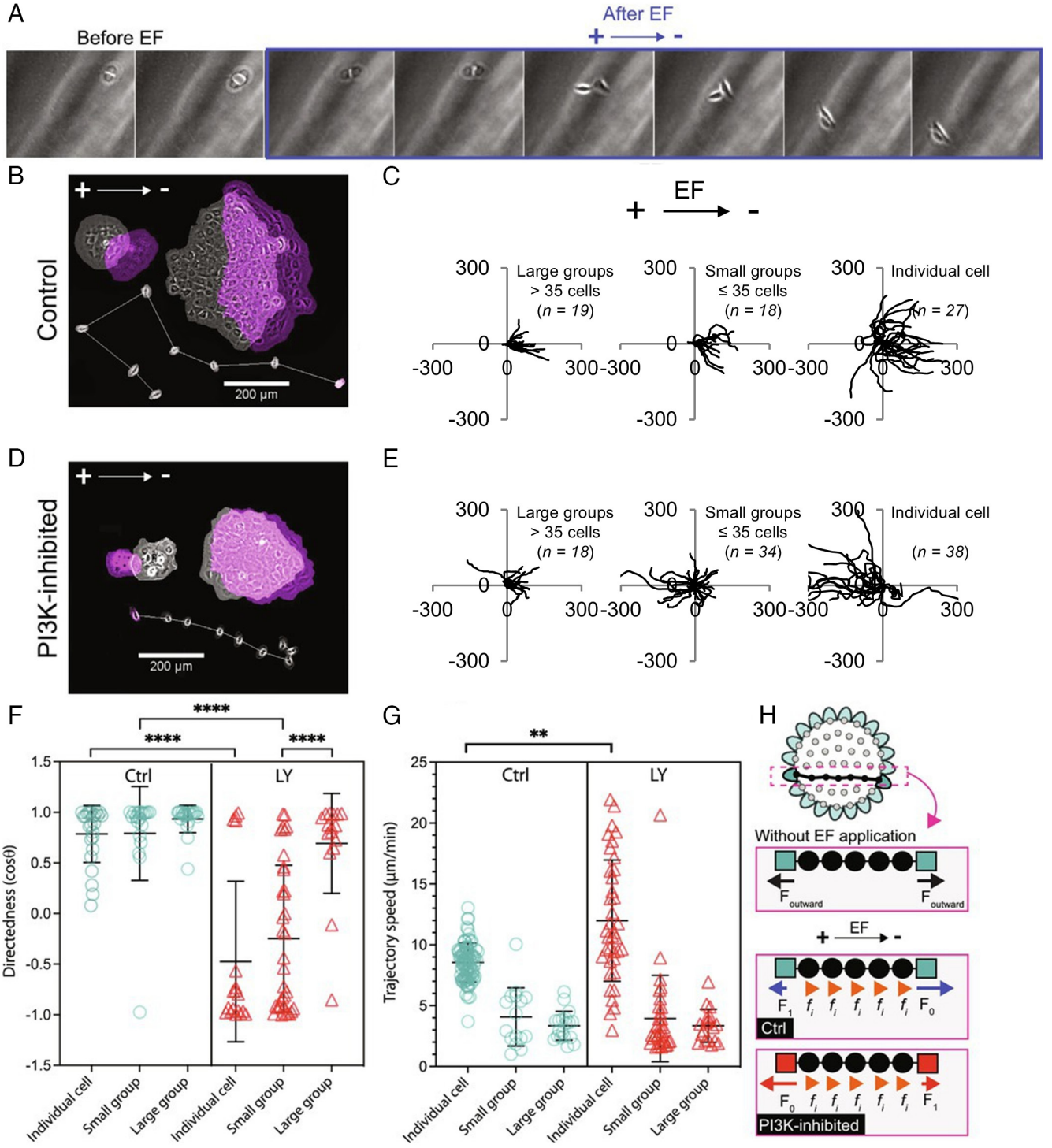

Fig. 1. EF guides individual keratocytes and groups to the cathode but directs individual cells and small groups to the anode in the presence of the PI3K inhibitor. (*A*) Snapshots of a pair of PI3K-inhibited cells imaged before and during 30 min after 1 V/cm EF application (see also Movie S1; cathode is at the *Right*). (*B*) Overlays of representative large (130 cells) and small (23 cells) groups and of one individual cell (with its migratory trajectory) before (gray) and 2 h after (magenta) 1 V/cm EF application. (*B*) Overlays of representative large (130 cells) and small (23 cells) groups and of one individual cell (with its migratory trajectory) before (gray) and 2 h after (magenta) 1 V/cm EF application. (*C*) Migratory trajectories of centroids of large (>35 and <400 cells, n = 19), small (≤35 cells, n = 18) groups, and individual (n = 27) keratocytes after applying 1 V/cm EF for 30 min. The distances along *x* and *y* axes are in μm. The tracks are recentered to the same starting point at the moment of EF application; trajectories are shown over 30 min after EF application. (*D*) Overlays of representative large (76 cells) and small (12 cells) and of one individual cell (with its migratory trajectory) before (gray) and 2 h after (magenta) 1 V/cm EF application in PI3K inhibition. (*E*) Migratory trajectories of centroids of large (n = 18), small (n = 34) groups, and individual (n = 38) keratocytes after applying 1 V/cm EF for 30 min in PI3K inhibition. The distances along *x* and *y* axes are in μm. The tracks are recentered to the same starting point at the moment of EF application; trajectories are shown over 30 min after EF application. (*F* and *G*) Comparison of the directedness (cosine of angle between the anode–cathode vector and the vector connecting the beginning (at the moment of EF application) and end (30 min after EF application) positions of the cell or group centroid; see *Methods*) and of the trajectory speed (speed of the centroid averaged over 30 min in EF, in μm/min) of the of individual cells, small and large groups, trajectories of which are shown in *C* and *E*. The quantification is done over a 30-min period post-EF application. Horizontal lines indicate the distribution mean with SD error bars. ****$P < 2.7e{-}6$; **$P < 2e{-}3$; ns, not significant ($P > 0.05$), one-way ANOVA (two-tailed *t* test). (*H*) One-dimensional theoretical model of propulsive forces in collective galvanotaxis.

As suggested by the two-cell behavior described above, without EF, the outer cells generate outward propulsive forces of equal magnitude, $F_{outward}$ (Fig. 1*H*). It would be natural to assume that the inner cells are not directional without EF, and then two outer cells in the 1D chain balance each other and the cohesive group is stationary. Based on the 2-PI3K-inhibited-cell behavior such, the magnitude of the anode-directed force of the anode-facing leader (left outer) cell, $-F_0$, is greater than the magnitude of the cathode-directed force of the trailer (right outer) cell, F_1 (Fig. 1*H*). (Positive/negative force is directed to the cathode on the right/anode on the left, respectively.) If in the presence of EF the inner cells are not directional, then the cell chain of any size would then experience the net anode-directed propulsive force $(-F_0 + F_1)$ and move to anode, contradicting the data. Thus, we posit that each inner cell generates a cathode-directed propulsion force $+f_i$, whether PI3K is inhibited or not. Similarly, it is natural to assume that in the chain of unperturbed cells, while each inner cell generates propulsion force $+f_i$, the leader cell is on the cathodal side and exerts the highest force, F_0, to the right, and the trailer cell is on the anodal side and exerts the lower force, $-F_1$, to the left. In principle, the forces' magnitudes could be different in the unperturbed and PI3K-inhibited cases, but for simplicity, we will keep them the same. Similarly, the inner cell propulsive forces can depend on the position inside the group (13), but for simplicity, we will keep them position independent. Several experimental studies indicated that leader (outer) cells exert higher forces than follower (inner) cells (4, 13, 48, 49), so we assume that $F_0 > F_1 > f_i$. If there are N inner cells in the chain, then the total force propelling the group is equal to $F_0 - F_1 + Nf_i$ in the unperturbed case, and to $(F_0 - F_1 + Nf_i)$ in the PI3K-inhibited case.

This simple 1D model makes several predictions. First, both unperturbed and PI3K-inhibited *large* groups are propelled with force approximately equal to Nf_i (if $N \gg 1$, then $(F_0 - F_1 + Nf_i) \approx (F_1 - F_0 + Nf_i) \approx Nf_i$). It is then logical to conclude that unperturbed and PI3K-inhibited *large* groups move with the same speed. Second, we know that large groups move to the cathode, whether Pi3K is inhibited or not, indicating that $f_i > 0$ in both cases. Thus, inner cells respond to EF by polarizing to the cathode, whether Pi3K is inhibited or not. Third, small unperturbed groups should move to the cathode, because if $F_0 > F_1$ and $f_i > 0$, then $(F_0 - F_1 + Nf_i) > 0$ for any N. However, small PI3K-inhibited groups should move to the anode, because if $F_0 > F_1$, then $(F_1 - F_0 + Nf_i) < 0$ for $N = 0$ and for small $N < (F_0 - F_1)/f_i$. Fourth, small unperturbed groups should move faster than small PI3K-inhibited groups of the same size because $|F_0 - F_1 + Nf_i| > |F_1 - F_0 + Nf_i|$ if $F_0 > F_1$ (simply speaking, because in unperturbed groups, inner and outer cells pull the group in the same, cathodal, direction, but in PI3K-inhibited groups, inner cells pull the group in the cathodal direction, while outer cells altogether push the group in the opposite direction). The predictions about equal speeds of large unperturbed and PI3K-inhibited groups and of speed of small unperturbed group being greater than speed of small PI3K-inhibited group agree with the measurements. Full mathematical analysis of the 1D model is presented in *SI Appendix*.

These predictions should be qualitatively valid in the realistic two-dimensional (2D) case, too. For a square group of N^2 cells, the number of outer cells scales as $\approx 4(N-1)$, while the number of inner cells scales as $\approx (N^2 - 4(N-1))$. Large groups, both unperturbed and PI3K-inhibited, move to the cathode, because in such groups, inner cells are in majority ($N^2 > 8(N-1)$) and win in the directional tug-of-war, while small groups ($N^2 < 8(N-1)$) are driven by the outer cell majority, which is either cathodal or anodal directed, depending on whether the group is unperturbed or PI3K-inhibited, respectively. It is interesting to note that the crossover from the inner to outer cell majority corresponds to the group size $N \approx 50$ ($N^2 \approx 8 \rightarrow N \approx 6.8$). Thus, we expect the crossover between the size-dependent directional behavior to occur for the group size between $36 = 6^2$ and $49 = 7^2$. Indeed, this turned out to be the characteristic threshold size at which we observe the directionality switch (*SI Appendix*, Fig. S2).

Large Groups Do Not Change Size and Shape upon Motility Initiation, While Smaller Groups Polarize and Lose Lamellipodia at the Rear Boundaries. To investigate the shapes and sizes of the galvanotactic cell groups, we excluded the groups which appeared polarized and moving directionally before EF was on and measured displacements, areas, and aspect ratios, from 30 min before EF was on to 30 min after EF was on, of such small (6 to 35 cells; we measure the number of the cells in groups as explained in *SI Appendix*, Fig. S4*C*) and large (37 to 200 cells) groups. The threshold of the 36-cell group was chosen based on the analysis in the previous section and data in *SI Appendix*, Fig. S2). Respective representative examples are shown in Fig. 2 *A*–*D* and Movies S2–S5, and statistics quantifying the EF-induced movements and shape changes can be gleaned from Fig. 2*I*.

Large cell groups of both unperturbed and PI3K-inhibited cells moved to cathode (Fig. 2 *A*, *C*, *E*, and *G*), almost without changing shape (Fig. 2 *E*, *G*, and *I*). Areas of these groups also changed relatively little (Fig. 2*I*). Note that the displacements of both large unperturbed and PI3K-inhibited groups were very similar to each other, as the simple 1D model predicted. Notably, most outer cells had lamellipodia protruding outward all around the group boundary, including the groups' rear (Fig. 2 *A* and *C*, *SI Appendix*, Fig. S5, and Movies S4 and S5).

Absolute values of the displacements of small unperturbed cell groups were greater than those of the small PI3K-inhibited groups, just as the simple 1D model predicted (Fig. 2*I*). Most notably, the aspect ratio of the small groups of both kinds changed significantly in EF—the groups became less roundish, shorter from rear to front and longer side-to-side (Fig. 2 *B*, *D*, *F*, *H*, and *I*). The group shape (Fig. 2 *B* and *D*), in fact, started to resemble the typical single motile cell shape. The reason for that was that most of the outer cells' lamellipodia at the rears of the groups were lost (Fig. 2 *B* and *D* and Movies S2 and S3), allowing the groups to pull their rear forward and inward, while the outer cells at the front and sides of the groups kept the lamellipodia stretching the group from side to side. The areas of the small groups decreased upon motility initiation going down more significantly than that of the large groups (Fig. 2*I*).

2D Mechanical Model with Velocity-Dependent Slippery Lamellipodial Clutch Explains the Data. To see whether the mechanical tug-of-war model could account for the data quantitatively and explain not only displacements but also shape changes of the motile groups, we turned to the 2D computational model (Fig. 3*A*). In the experiments, we observed that at the time scale of tens of minutes, the order of cells within the groups remained fixed—individual cells did not exchange neighbors, thus, the cells in the groups were cohesive with their neighbors, and so we modeled the mechanical links between neighboring cells as elastic. Each cell was assumed to resist its propulsion force by generating viscous-like resistance (13) characterized by the effective drag coefficient, same for all cells. Without EF, inner

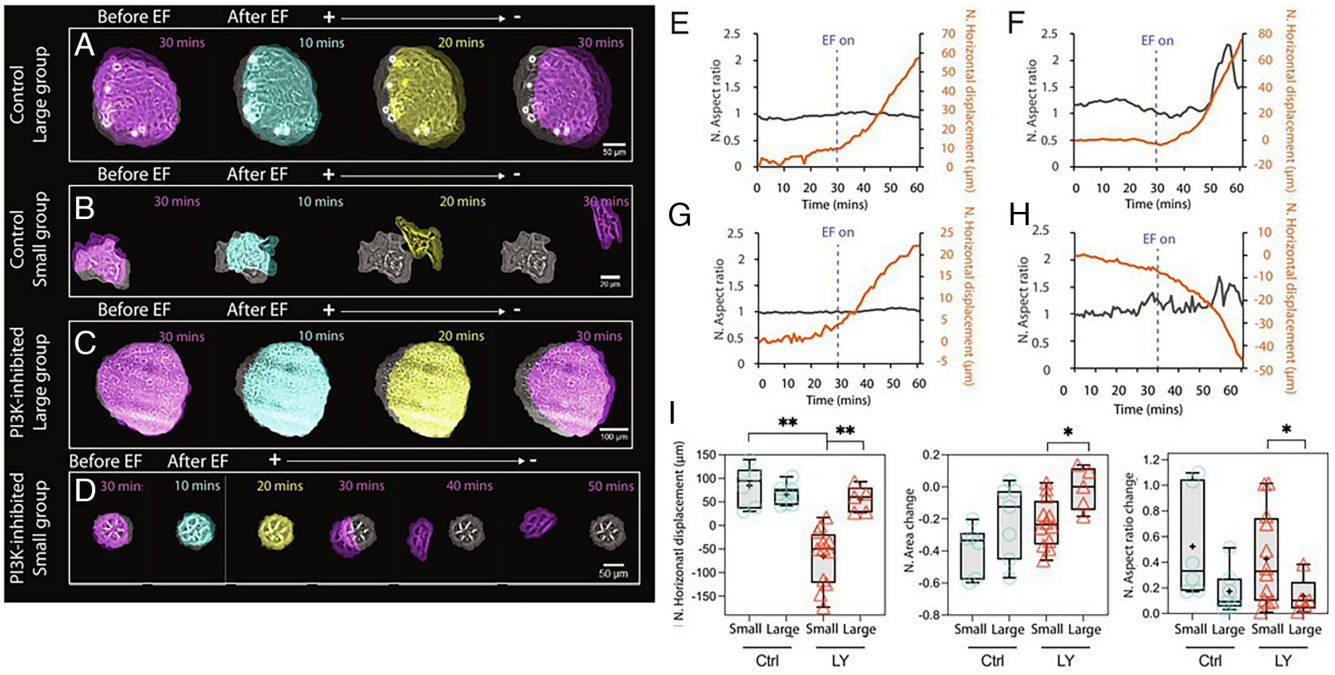

Fig. 2. Significant morphological changes observed in small groups but not in larger groups. (*A*–*D*) Overlays of representative large and small groups each containing 68, 8, 102, and 7 cells, respectively, earlier (gray) and later (color) in control and PI3 inhibited cases. A 1 V/cm EF is applied with the cathode to the *Right*. See also Movies S2–S5. (*E*–*H*) Normalized (by its value before EF application) aspect ratio and displacement along the EF axis over time in both large (*E* and *G*) and small (*F* and *H*) groups in (*E* and *F*) control and (*G* and *H*) PI3K-inhibited cases. 1 V/cm EF is applied at the 30-min mark. (*I*) Comparisons of displacement, area, and aspect ratio changes induced by EF in the absence or presence of the PI3K inhibitor (LY). Displacement along the EF axis is reported 30 min after 1 V/cm EF application in large (n = 6) and small (n = 7) groups in the absence (Ctrl) and in large (n = 12) and small (n = 5) groups in the presence (LY) of the PI3K inhibitor. The normalized area and normalized absolute values of aspect ratio changes are reported from right before to 30 min after 1 V/cm EF application. $^{**}P < 3.6e{-}5$; ns, not significant ($P > 0.05$), one-way ANOVA (two-tailed *t* test). $^{*}P < 0.04$; ns, not significant ($P > 0.05$), one-way ANOVA (two-tailed *t* test. Horizontal lines inside the boxes indicate distribution median, while the plus symbols show the mean. Tops and bottoms of each box indicate 75% (q_3) and 25% (q_1) percentiles, respectively. The whiskers extend to the highest and lowest values.

cells in the model did not generate any propulsive force, while the outer cells generated equal-magnitude protrusive forces directed outward perpendicularly to the local group edge (Fig. 3*A*) (as in refs. 7 and 39). With EF, each inner cell in the model generated a constant cathode-oriented propulsion force, whether Pi3K is inhibited or not, while the outer cells generated the geometry- and PI3K-dependent propulsion forces, as follows. Outer cells, lamellipodia of which faced the cathode, generated a cathode-oriented force F_0 (unperturbed) or F_1 (unperturbed) (Fig. 4*A*). Outer cells, lamellipodia of which faced the anode, generated an anode-oriented force F_1 (unperturbed) or F_0 (unperturbed). Finally, we introduced the "slippery clutch" mechanism, which is similar to models in refs. 43 and 46 and which is suggested by our observations: When the group moves directionally and the lamellipodia of the outer cells are dragged by the group against the direction, in which these lamellipodia try to protrude, these lamellipodia get destabilized, if the speed of the movement in the "wrong" direction exceeds the threshold.

In the *SI Appendix*, we describe the quantitative details of the model and the search for its mechanical parameters informed by the experimental measurements. Numerical simulations of the model with the constrained parameters reproduced the experimentally observed shapes and movements in four cases of small and large, unperturbed, and PI3K-inhibited (Fig. 3*B* and Movie S6): Small PI3K-inhibited groups moved to the anode; in the three other cases, the groups moved to the cathode. The small groups moved faster than the large groups, because the outer cells generate greater net propulsive forces than the inner cells, and in small groups the minority of the inner cells effectively slows the groups down less than the majority of the inner cells in large groups. In addition, because the small groups move faster, lamellipodia at their rears destabilize, further decreasing the resistance and accelerating the groups. This lamellipodia destabilization effect explains the more significant decrease of the group area and increase of the group aspect ratio for the small groups: The outer cells at the rear are not pulled outward against the group direction, allowing the effectively elastic mesh of the inner cells to contract inward, shrinking the rear-to-front distance in the group and decreasing its area. We calculated the displacements, areas, and aspect ratios in these four cases, and the results (*SI Appendix*, Table S2) display the same qualitative trends as the experimental measurements (Fig. 3*I*).

Bidirectional Polarization of Complex-Shaped Group Confirms a Model Prediction. The 2D model also makes a simple prediction about a bilobed-shaped group of PI3K-inhibited cells, with two lobes connected by a narrow cell corridor (Fig. 4*A* and Movie S7): If the smaller lobe's size is less than the critical size at which the group directionality switches from the anode to cathode, while the greater lobe's size is larger than critical, then the lobes would move oppositely to each other in EF, deforming the group shape. We simulated a group of such shape and indeed found that this intuition is correct (Fig. 4*A*). After such initial bidirectional deformation, the greater lobe prevailed in the tug-of-war and started to drag the whole group to the cathode (Fig. 4*A*). With a nonlinear slip-like response of cell–cell adhesions, the tug-of-war leads to breaking apart of the cluster into separate lobes with opposite velocities (*SI Appendix*). The cell groups in the experiment tend to stay roundish in the absence of EF, likely because an effective boundary tension generated by a collective myosin contraction of the rears of the outer cells, but we found one large group of PI3K-inhibited cells of the sufficiently elongated shape (Fig. 4*B*) that allowed us to test this prediction. We observed

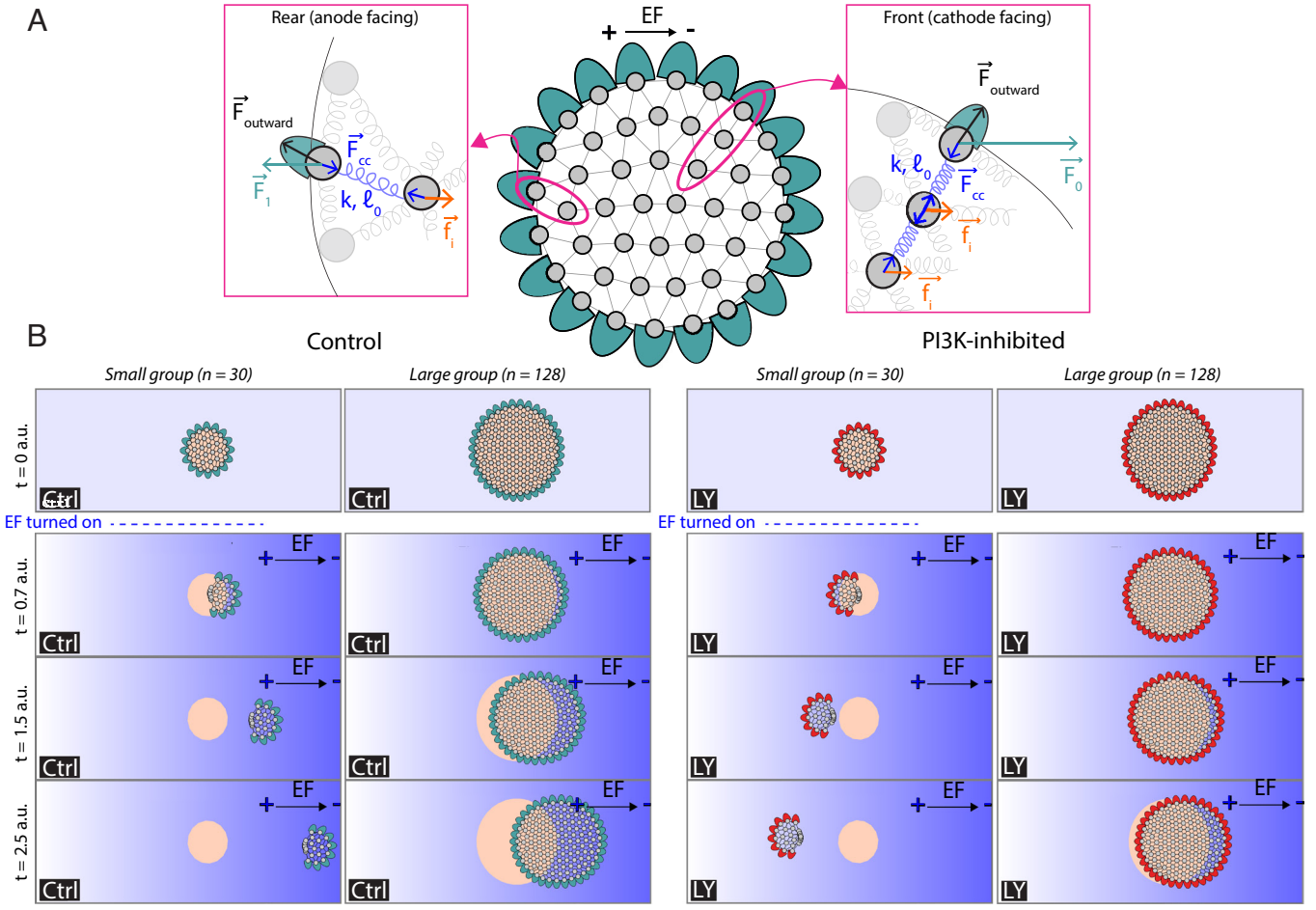

Fig. 3. 2D model with propulsion forces that depend on the cell position within the group and on the PI3K signaling. (*A*) Diagram illustrating all components in the model, including cell–cell forces, EF-induced propulsion forces, and outward protrusive forces for outer cells in the outward normal direction. The cell–cell interaction is modeled with an elastic spring with nonzero resting length and stiffness. For unperturbed (Ctrl) groups, the outer cells (cyan) sense EF leading them to the cathode, and the propulsion forces at the front of the group are larger than those at the back (blue arrows). The inner cells generate propulsion forces pointing to the cathode (orange arrows). For the PI3K-inhibited group, the propulsion forces of the outer cells pointing to the anode are larger than those at the front (red arrows), while the active forces of inner cells are the same as in the unperturbed group (orange cells). (*B*) Simulation snapshots of the model at four distinct timepoints: Initially (t = 0 a.u.) and after application of the EF at t = 0.5 a.u. (t = 0.7, 1.5, and 2.5 a.u) (Movie S6). Cathode is always to the right. The initial configuration is shown in an orange overlay, while the later configuration is shown with individual cells (gray) and lamellipodia of engaged outer cells (cyan in control groups and red in PI3K-inhibited groups).

that in the first 15 min after EF was switched on, all parts of the group moved to the cathode, but the "upper" part of the group less directionally so, than the rest of the group, which predeformed the group into the bilobed shape (Movie S8). In the next 15 min, the smaller lobe moved toward the anode, oppositely to the greater lobe that continued to the cathode, as predicted. After that, the cell corridor between the lobes that was narrowing during the bidirectional deformation of the group broke, and the two resulting groups went in their opposite respective directions. This last break-up part of the process is not predicted by the model because of the linear elastic character of the cell–cell links in the model, but it is easy to imagine that introducing more complex non-linear dynamic links will lead to accounting for this breakage. Another large and elongated group provides one more example of this phenomenon: While the bulk of the group polarizes to the cathode, two small subgroups split from the anodal edge of the main group and initiate movement to the anode (Movie S9).

Discussion

We found that while single unperturbed cells and groups of all sizes move to the cathode, single and small (tens of cells) groups of PI3K-inhibited cells move to the anode, but larger (hundreds of cells) groups still move to the cathode. Groups of the unperturbed cells shift along the EF vector more than PI3K-inhibited cell groups of similar sizes. Smaller groups of the unperturbed/PI3K-inhibited cells are slightly faster than larger groups of the unperturbed/PI3K-inhibited cells, respectively. Large groups of both unperturbed and PI3K-inhibited cells undergo little change in shape and area after initiating the EF-induced motility. When motile, outer cells of such groups had lamellipodia protruding outward all around the group's periphery. In contrast, small groups of both unperturbed and PI3K-inhibited cells underwent a more significant decrease in area and shape after initiating the EF-induced motility. Such groups also polarized, so that lamellipodia of the outer cells at the front and sides of the small groups were prominent, while those of the outer cells at the rear of the small groups were largely lost, so the small groups' shapes looked like giant single cells.

We propose the following mechanistic explanation of the data (Fig. 4*C*): inner cells always, independently of the cells' PI3K signaling, tend to go to the cathode, while the outer cells behave directionally like single cells. According to this model, unperturbed cell groups of all sizes are driven to the cathode, as are all cells in the group. The directionality of PI3K-inhibited cell groups is determined by a mechanical tug-of-war between the cathode-driven

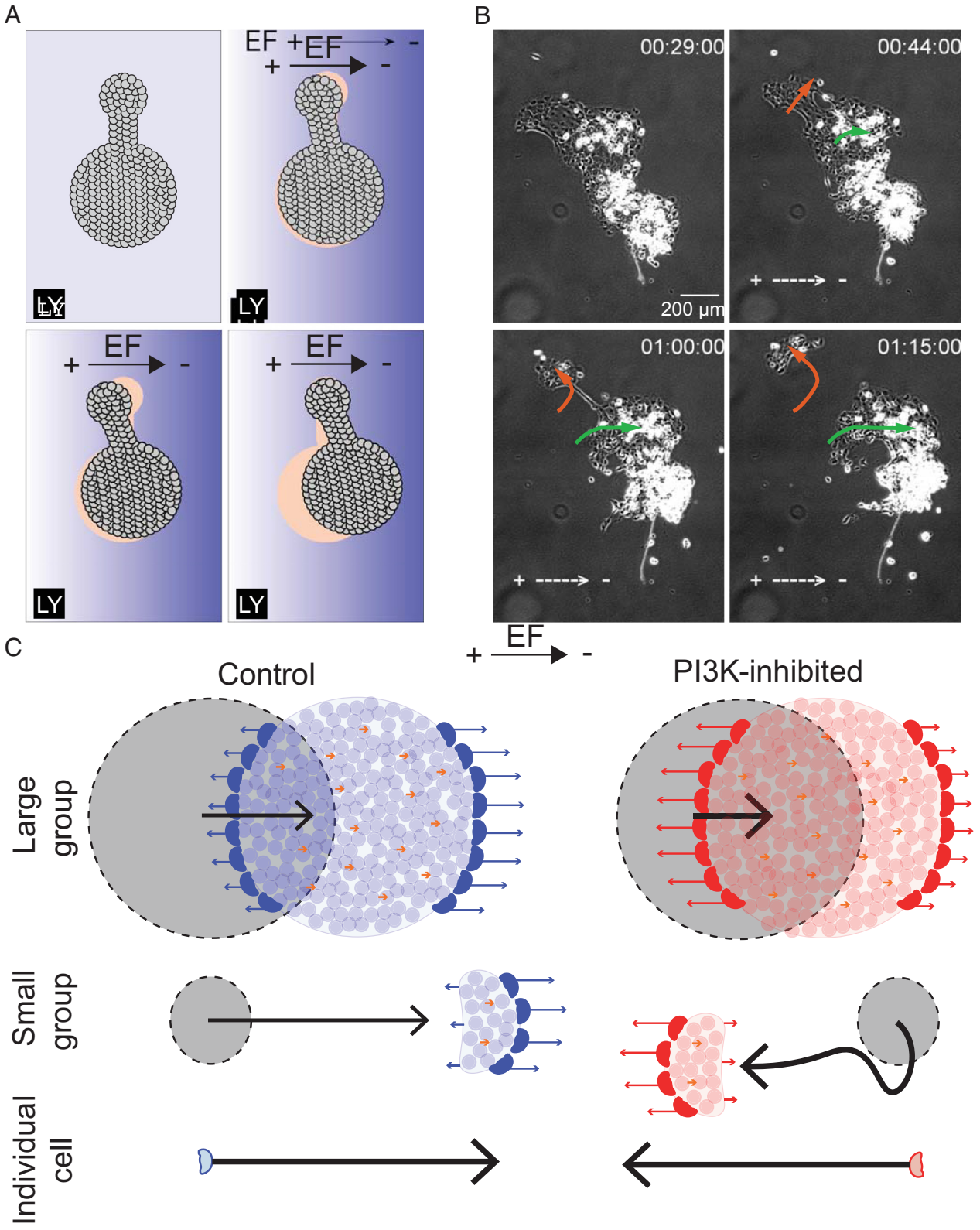

Fig. 4. In the presence of 100 μM of the PI3K inhibitor, small group of cells splits off from a larger cell cluster. (*A*) Simulation snapshots of a dumbbell-shaped cluster of cells with n = 270. The orange background overlay shows the initial configuration. In the simulation, the cell–cell links, modeled as elastic bonds, cannot rupture (Movie S7). (*B*) Snapshots of a large group containing 221 cells with a 1 V/cm EF in the presence of 100 μM of the PI3K inhibitor compound (Movie S8). Arrows indicate the displacement of the original group (green) and a small group containing 25 cells (orange) that eventually splits off. The EF is applied at the 30-min mark with cathode at the *Right*. (Scale bar, 200 μm.) (*C*) Hypothesized tug-of-war in cell groups in the presence of EF. The magenta arrow indicates the migration direction for large and small groups and individual cells. The polarization vectors are shown for edge (black) and inner (orange) cells in large and small groups. Note that the edge polarization signals are stronger in the single or edge cell compared to the inner cell.

inner and anode-biased outer cells. In larger groups, the former are the majority; they win, and the group migrates to cathode. In smaller groups, the latter are the majority; they win, and the group migrates to the anode. Furthermore, if one additional mechanical assumption is made in the model—lamellipodia of outer cells at the rear of the group, dragged by the group's majority against their

local protrusion directions, are destabilized if the group speed is faster than a threshold—then the model also able to explain semiquantitatively not only groups' speeds, but also their shapes and polarization states. In agreement with this model, in rare large PI3K-inhibited cell groups with complex shapes, small and relatively isolated from the main part of the group cell clusters at the groups' periphery showed tendency to go to the anode, oppositely to the cathodal direction of the main part of the group.

The main premise of our model—that directionalities of the inner and outer cells are different—is supported by several observations of cohesive groups of other cell types (8, 11, 50). What mechanisms could be behind this difference? It could be based on significant distinctions in cytoskeletal organizations in inner and outer cells (31), the most prominent of which is large lamellipodia of the outer cells (Figs. 1 *A* and 2 *B* and *D*). Inner cells have only cryptic lamellipodia (49, 51); active lamellipodia of these cells are suppressed by physical coupling to neighboring cells on all sides (26). Another distinction is that the outer cells are strongly polarized, while it was shown that myosin distribution in keratocytes inside the cell sheet is unpolarized (31). (Inhibition of myosin was very informative for deciphering rules of galvanotaxis for single keratocyte cells (30), but not for the cell groups, because upon inhibition of myosin, cohesion between the individual cells in the groups is lost (31, 33); therefore, we did not use this perturbation in this study.) Different cytoskeletal structures could interpret extracellular signals in divergent ways (52).

Another possibility stems from different sizes of large lamellipodia of the outer cells and small cryptic lamellipodia of the inner cells (49) and potential signal strength dependence on cell size (29, 42). Specifically, considering that EF induces a gradient of charged motile proteins across the cell surface (29), the ratio of the charged motile protein concentrations at the cathodal and anodal sides of the lamellipodia is on the order of $exp(qEL/k_{BT})$, where q is an effective protein net charge, E is EF amplitude, L is the lamellipodial width, and k_{BT} is molecular thermal energy. This exponential factor could translate into great size-dependent signal differences, so that larger outer cell lamellipodia perceive a much stronger EF signal that could trigger some intracellular signaling pathways which are not activated by weaker subthreshold EF signal in smaller inner cells. Notably, small lamellipodial fragments have opposite directionality in EF compared to large whole keratocytes (30). Finally, considering the likelihood of several pathways polarizing cells in EF (30), one could hypothesize that the EF signal is transduced by three independent additive pathways. For example, the first pathway weakly polarizes the cell body to the cathode, the second one strongly polarizes the lamellipodium to the cathode in a PI3K-dependent way, and the third one strongly polarizes the lamellipodium to the anode in a PI3K-independent way. [Of note, active PI3K was observed to localize to the leading edge of leader cells, but not in follower cells in the group (50)]. Then, in the inner cell, the first pathway becomes dominant orienting the cell to the cathode independent of the PI3K signaling. In the unperturbed outer cell, the effects of the second and third pathways cancel each other, and the first pathway, again, orients the cell to the cathode. Finally, in the PI3K-inhibited outer cell, the second pathway does not work, and the strong third pathway wins against the weak first pathway orienting the cell to the anode.

An interesting open question is how general the size-dependent directionality phenomenon is. One study (53) reported that lymphocyte clusters always followed the chemical gradient, independent of its steepness, while single cells reversed directionality for very steep gradients. It is well known in the chemotaxis that individual cells can be turned around by some chemical perturbations (54), but how cell groups will behave under the same perturbations is unclear. Another important question is whether there are physiological implications of the reported galvanotaxis phenomenon. When fish skin is injured, keratocyte cell groups migrate to repair the wound and re-epithelialization of these wounds is extremely rapid (55). Considering that these cell groups follow local EF (18) and that PI3K activity levels can vary in cells engaged in collective locomotion (56), it is to be expected that complex, size-dependent directionality affects wound healing.

There is much complexity of the collective galvanotactic response that our study did not address. There are relatively slow (hours-scale) processes of adaptation of the group migration to EF manifested in gradual slowing down of the migration (31, 33, 57), and in gradual redistribution of global stresses in the groups (26). Effects of EF on cell motility are more nuanced than orienting and calibrating cell propulsion forces (41). Other sources of complexity are natural cell-to-cell variabilities in directional responses, nontrivial rheology of the cell clusters, and stochastic effects in collective directional sensing (58). Another complex possibility is that the cells inside the group are integrated into supracellular sheets irreducible to autonomous mechanochemical units (13). Indeed, integrated cytoskeletal networks (31), intercellular stresses (26), and global bioelectric gradients (59) in migrating cell groups were reported. Last, but not least, there is a subtle interplay between polarization vector and propulsion force in cells, which our model does not take into account; for example, it is possible that main driving force arises from cells inside the group, while outer cells are mainly giving direction (60). Future research will shed light on the impact of these complexities on collective cell galvanotaxis.

Conclusion

Individual fish keratocyte cells migrate to the cathode, while inhibition of PI3K reverses single cells to the anode. Chemically unperturbed cell groups of any size move to the cathode. Large groups of PI3K-inhibited cells move to the cathode, while small groups of PI3K-inhibited cells move to the anode. These results can be explained by the model according to which inner cells, whether unperturbed or PI3K-inhibited, always have tendency to move to the cathode, while peripheral cells in the group behave as single cells: They are directed to the cathode if uninhibited, but biased to the anode, if PI3K-inhibited. A mechanical tug-of-war between the inner and edge cells directs larger groups with majority of the inner cells to the cathode and smaller groups with majority of the outer cells to the anode.

Methods

Primary Culture of Keratocyte Groups and Single Cells. Adult zebrafish (strain AB) were obtained from the UC Davis Zebrafish facility. All experiments were conducted in accordance with the UC Davis Institutional Animal Use and Care Committee protocol 16478. Scales were removed from zebrafish flanks and allowed to adhere to the bottom of EF chambers (31, 61). The scales were covered by a glass 22-mm coverslip with a stainless-steel nut on the top and cultured at room temperature in Leibovitz's L-15 media (Gibco BRL), supplemented with 14.2 mM HEPES pH 7.4, 10% Fetal Bovine Serum (Invitrogen), and 1% antibiotic-antimycotic (Gibco BRL). Scales were removed gently once an epithelial sheet forms, which usually takes 24 to 48 h. Cell groups of various sizes and shapes separated from the epithelial sheet spontaneously and migrated away; these groups were used in the experiments with EF. To isolate single cells, groups of keratocytes that migrated off the scale were digested by a brief treatment with 0.25% Trypsin/0.02 EDTA solution (Invitrogen) in phosphate-buffered saline and then kept on ice until use (61, 62).

Pharmacological Perturbation Experiments. Drugs were added in the culture medium in the following concentration: 0.1% dimethyl sulfoxide (Sigma, Cat# 900185) as drug control, 50 or 100 μM LY294002 (Sigma, Cat# 440202). Subsequent experiments were implemented in the presence of each of these drugs within 15 min of incubation.

EF Application and Time-Lapse Recording. The EFs were applied as previously described (63, 64) in custom-made electrotaxis chambers to minimize heating during experiment. To eliminate toxic products from the electrodes that might be harmful to cells, agar salt bridges made with 1% agar gel in Steinberg's salt solution were used to connect silver/silver chloride electrodes in beakers of Steinberg's salt solution to pools of excess medium at either side of the chamber (*SI Appendix*, Fig. S4*A*). Our previous work and data reported in *SI Appendix*, Fig. S1 demonstrated that a threshold EF magnitude is required to trigger galvanotactic responses in both individual cells (25) and cell groups (22). Increasing the EF strength enhances both the migration velocity and the ability to polarize (22); both the critical group size for directional transition and group velocity are influenced by the EF magnitude (34). In this study, we focused on a fixed EF strength based on physiological range and previous studies (31). In most experiments, an EF of 1 V/cm was used unless otherwise indicated. The actual voltage is measured by a voltmeter before and after each experiment. Phase contrast images were captured by a Zeiss Observer Z1 (Carl Zeiss) equipped with a QuantEM:512SC EMCCD camera (Photometrics). Time-lapse experiments were performed using MetaMorph NX software controlling a motorized scanning stage (Carl Zeiss). Typically, in each experiment, overlapped fields covering a whole cell group were captured sequentially. Images were taken at 30 or 60 s interval at room temperature for up to 60 min unless stated otherwise.

Image Processing and Data Analysis/Presentation. Time-lapse images were imported into ImageJ and stitched by using Grid/Collection Stitching plugin (*SI Appendix*, Fig. S4*B*). To quantify single-cell and collective group motility, we extracted the trajectory of each object using an automatic/manual tracking tool (31, 65, 66). Directedness was defined as $\cos(\theta)$, where θ is the angle between the EF vector and the vector connecting the centroids of the cell/group in the initial and final positions (38, 67). To quantify cell/group migration, x and y coordinates of single cells and of the groups' centroid were measured in each image [the origin (0,0) was the initial coordinate] in the image stack, with the x-axis parallel to the EF, as described previously (31). The (x, y) trajectory data were imported into ImageJ chemotaxis tool plugin and rescaled to physical dimensions based on pixel sizes. The trajectory speed was computed by dividing incremental centroid displacement over the respective time interval and then averaging this momentous speed over the whole trajectory.

Morphological Characterization and Quantification. Cell numbers in each group were either manually counted (for the groups with less than 100 cells) using ImageJ particle analysis tool (*SI Appendix*, Fig. S4 *C*, *Left*) or calculated based on the area fractions (for the groups with more than 100 cells or difficult to count, *SI Appendix*, Fig. S4 *C*, *Right*). Groups were then either manually outlined in ImageJ or processed by using a custom-written Matlab codes to outline with extracted contours (68, 69). Briefly, we used Matlab edge detection and a basic morphology function to outline cell groups in the phase contrast image. In most cases, we had to use the Lasso tool in Photoshop (Adobe) to manually draw the group shape. Polygonal outlines extracted from the binary images were plotted in Celltool, an open-source software (70). Geometric features of each cell group including centroid, aspect ratio, and area (*SI Appendix*, Fig. S4*D*) were measured directly from the polygons by using standard formulas (53).

Statistics and Reproducibility. All experiments were repeated and produced similar results. In most cases, a representative experiment is shown, unless stated otherwise. Data are presented as means ± SE. To compare group differences (EF vs. no EF or drug treatment vs. no treatment), either chi-squared test, or paired/unpaired, two-tailed Student's *t* test were used. A *P* value less than 0.05 was considered as significant.

Modeling. Details of the computational model are described in the *SI Appendix*.

Data, Materials, and Software Availability. Numerical codes used to simulate the computational model can be accessed at https://github.com/CoposGroup/Galvanotaxis (71). All study data are included in the article and/or supporting information.

ACKNOWLEDGMENTS. This work was supported by NSF grant DMS2209494 to C.C., US Army Research Office grant W911NF-17-1-0417 to A.M., by Air Force Office of Scientific Research grant FA9550-16-1-0052 to M.Z. (Program PI: Wolfgang Losert), and by NIH grant EY 019101 to M.Z.

1. P. Friedl, D. Gilmour, Collective cell migration in morphogenesis, regeneration and cancer. *Nat. Rev. Mol. Cell Biol.* **10**, 445–457 (2009).
2. E. Scarpa, R. Mayor, Collective cell migration in development. *J. Cell Biol.* **212**, 143–155 (2016).
3. A. S. Kennard, J. A. Theriot, Osmolarity-independent electrical cues guide rapid response to injury in zebrafish epidermis. *Elife* **9**, e62386 (2020).
4. D. Mohammed *et al.*, Substrate area confinement is a key determinant of cell velocity in collective migration. *Nat. Phys.* **858**, 858–866 (2019).
5. B. Szabo *et al.*, Phase transition in the collective migration of tissue cells: Experiment and model. *Phys. Rev. E.* **74**, 061908 (2006).
6. L. J. Schumacher, P. M. Kulesa, R. McLennan, R. E. Baker, P. K. Maini, Multidisciplinary approaches to understanding collective cell migration in developmental biology. *Open Biol.* **6**, 160056 (2016).
7. B. A. Camley, J. Zimmermann, H. Levine, W.-J. Rappel, Emergent collective chemotaxis without single-cell gradient sensing. *Phys. Rev. Lett.* **116**, 098101 (2016).
8. K. Copenhagen *et al.*, Frustration-induced phases in migrating cell clusters. *Sci. Adv.* **4**, eaar8483 (2018).
9. T. Omelchenko, J. M. Vasiliev, I. M. Gelfand, H. H. Feder, E. M. Bonder, Rho-dependent formation of epithelial "leader" cells during wound healing. *Proc. Natl. Acad. Sci. U.S.A.* **100**, 10788–10793 (2003).
10. M. Reffay *et al.*, Interplay of RhoA and mechanical forces in collective cell migration driven by leader cells. *Nat. Cell Biol.* **16**, 217–223 (2014).
11. D. J. Cohen, W. J. Nelson, M. M. Maharbiz, Galvanotactic control of collective cell migration in epithelial monolayers. *Nat. Mater.* **13**, 409–417 (2014).
12. X. Trepat, J. J. Fredberg, Plithotaxis and emergent dynamics in collective cellular migration. *Trends Cell Biol.* **21**, 638–646 (2011).
13. L. Rossetti *et al.*, Optogenetic generation of leader cells reveals a force-velocity relation for collective cell migration. *Nat. Phys.* **20**, 1659–1669 (2024).
14. A. Shellard, A. Szabó, X. Trepat, R. Mayor, Supracellular contraction at the rear of neural crest cell groups drives collective chemotaxis. *Science* **362**, 339–343 (2018).
15. A. E. Wolf, M. A. Heinrich, I. B. Breinyn, T. J. Zajdel, D. J. Cohen, Short-term bioelectric stimulation of collective cell migration in tissues reprograms long-term supracellular dynamics. *PNAS Nexus.* **1**, pgac002 (2022).
16. J. P. Campanale, D. J. Montell, Who's really in charge: Diverse follower cell behaviors in collective cell migration. *Curr. Opin. Cell Bio.* **81**, 102160 (2023).
17. M. Levin, G. Pezzulo, J. M. Finkelstein, Endogenous bioelectric signaling networks: Exploiting voltage gradients for control of growth and form. *Annu. Rev. Biomed. Eng.* **19**, 353–387 (2017).
18. Y. Sun *et al.*, Infection-generated electric field in gut epithelium drives bidirectional migration of macrophages. *PLoS Biol.* **17**, e3000044 (2019).
19. F. Ferreira, G. Luxardi, B. Reid, M. Zhao, Early bioelectric activities mediate redox-modulated regeneration. *Development* **143**, 4582–4594 (2016).
20. A. Guo *et al.*, Effects of physiological electric fields on migration of human dermal fibroblasts. *J. Invest. Dermatol.* **130**, 2320–2327 (2010).
21. F. Chang, N. Minc, Electrochemical control of cell and tissue polarity. *Annu. Rev. Cell Dev. Biol.* **30**, 317–336 (2014).
22. L. Li *et al.*, E-cadherin plays an essential role in collective directional migration of large epithelial sheets. *Cell Mol. Life Sci.* **69**, 2779–2789 (2012).
23. M. L. Lalli, A. R. Asthagiri, Collective migration exhibits greater sensitivity but slower dynamics of alignment to applied electric fields. *Cell Mol. Bioeng.* **8**, 247–257 (2015).
24. T. J. Zajdel, G. Shim, L. Wang, A. Rossello-Martinez, D. J. Cohen, SCHEEPDOG: Programming electric cues to dynamically herd large-scale cell migration. *Cell Syst.* **10**, 506–514.e3 (2020).
25. Y. Zhang *et al.*, Collective cell migration has distinct directionality and speed dynamics. *Cell Mol. Life Sci.* **74**, 3841–3850 (2017).
26. Y. Cho, M. Son, H. Jeong, J. H. Shin, Electric field-induced migration and intercellular stress alignment in a collective epithelial monolayer. *Mol. Biol. Cell.* **29**, 2292–2302 (2018).
27. A. Mogilner, E. L. Barnhart, K. Keren, Experiment, theory, and the keratocyte: An ode to a simple model for cell motility. *Semin. Cell Dev. Biol.* **100**, 143–151 (2019).
28. M. S. Cooper, M. Schliwa, Motility of cultured fish epidermal cells in the presence and absence of direct current electric fields. *J. Cell Biol.* **102**, 1384–1399 (1986).
29. G. M. Allen, A. Mogilner, J. A. Theriot, Electrophoresis of cellular membrane components creates the directional cue guiding keratocyte galvanotaxis. *Curr. Biol.* **23**, 560–568 (2013).
30. Y. Sun *et al.*, Keratocyte fragments and cells utilize competing pathways to move in opposite directions in an electric field. *Curr. Biol.* **23**, 569–574 (2013).
31. J. L. Rapanan, K. E. Cooper, K. J. Leyva, E. E. Hull, Collective cell migration of primary zebrafish keratocytes. *Exp. Cell Res.* **326**, 155–165 (2014).
32. L. Huang, P. Cormie, M. A. Messerli, K. R. Robinson, The involvement of Ca2+ and integrins in directional responses of zebrafish keratocytes to electric fields. *J. Cell Physiol.* **219**, 162–172 (2009).
33. Y. Sun *et al.*, Electric field–guided collective motility initiation of large epidermal cell groups. *Mol. Biol. Cell* **34**, ar48 (2023).
34. M. Zhao *et al.*, Electrical signals control wound healing through phosphatidylinositol-3-OH kinase-gamma and PTEN. *Nature* **442**, 457–460 (2006).
35. C. Carmona-Fontaine *et al.*, Contact inhibition of locomotion in vivo controls neural crest directional migration. *Nature* **456**, 957–961 (2008).
36. A. J. Lomakin *et al.*, Competition for actin between two distinct F-actin networks defines a bistable switch for cell polarization. *Nat. Cell Biol.* **17**, 1435–1445 (2015).

37. C. Copos, A. Mogilner, A hybrid stochastic–deterministic mechanochemical model of cell polarization. *Mol. Biol. Cell* **31**, 1551–1649 (2020).
38. C. D. McCaig, B. Song, A. M. Rajnicek, Electrical dimensions in cell science. *J. Cell Sci.* **122**, 4267–4276 (2009).
39. B. A. Camley, Collective gradient sensing and chemotaxis: Modeling and recent developments. *J. Phys. Condens. Matter.* **30**, 223001 (2018).
40. L. Tweedy, D. A. Knecht, G. M. Mackay, R. H. Insall, Self-generated chemoattractant gradients: Attractant depletion extends the range and robustness of chemotaxis. *PLoS Biol.* **14**, e1002404 (2016).
41. T. P. Prescott, K. Zhu, M. Zhao, R. E. Baker, Quantifying the impact of electric fields on single cell motility. *Biophys. J.* **120**, 3363–3373 (2021).
42. I. Nwogbaga, A. Hyun Kim, B. A. Camley, Physical limits on galvanotaxis. *Phys. Rev. E* **108**, 064411 (2023).
43. J. E. Ron, P. Monzo, N. C. Gauthier, R. Voituriez, N. S. Gov, One-dimensional cell motility patterns. *Phys. Rev. Res.* **2**, 033237 (2020).
44. K. Hennig *et al.*, Stick-slip dynamics of cell adhesion triggers spontaneous symmetry breaking and directional migration of mesenchymal cells on one-dimensional lines. *Sci. Adv.* **6**, eaau5670 (2020).
45. P. Sens, Stick–slip model for actin-driven cell protrusions, cell polarization, and crawling. *Proc. Natl. Acad. Sci. U.S.A.* **117**, 24670–24678 (2020).
46. R. Alonso-Matilla, P. P. Provenzano, D. J. Odde, Optimal cell traction forces in a generalized motor-clutch model. *Biophys. J.* **122**, 3369–3385 (2023).
47. B. Merchant, L. Edelstein-Keshet, J. J. Feng, A Rho-GTPase based model explains spontaneous collective migration of neural crest cell clusters. *Dev. Biol.* **444**, S262–S273 (2018).
48. K. Suffoletto, D. Jetta, S. Z. Hua, E-cadherin mediated lateral interactions between neighbor cells necessary for collective migration. *J. Biomech.* **71**, 159–166 (2018).
49. C. Okimura *et al.*, Leading-edge elongation by follower cell interruption in advancing epithelial cell sheets. *Proc. Natl. Acad. Sci. U.S.A.* **119**, e2119903119 (2022).
50. N. Yamaguchi, T. Mizutani, K. Kawabata, H. Haga, Leader cells regulate collective cell migration via Rac activation in the downstream signaling of integrin beta1 and PI3K. *Sci. Rep.* **5**, 7656 (2015).
51. R. Farooqui, G. Fenteany, Multiple rows of cells behind an epithelial wound edge extend cryptic lamellipodia to collectively drive cell-sheet movement. *J. Cell Sci.* **118**, 51–63 (2005).
52. P. A. Janmey, The cytoskeleton and cell signaling: Component localization and mechanical coupling. *Physiol. Rev.* **78**, 763–781 (1998).
53. G. Malet-Engra *et al.*, Collective cell motility promotes chemotactic prowess and resistance to chemorepulsion. *Curr. Biol.* **25**, 242–250 (2015).
54. J. Xu *et al.*, Divergent signals and cytoskeletal assemblies regulate self-organizing polarity in neutrophils. *Cell* **114**, 201–214 (2003).
55. L. Sveen, C. Karlsen, E. Ytteborg, Mechanical induced wounds in fish–A review on models and healing mechanisms. *Rev. Aquacult.* **12**, 2446–2465 (2020).
56. S. Deng *et al.*, PI3K/AKT signaling tips the balance of cytoskeletal forces for cancer progression. *Cancers* **14**, 1652 (2022).
57. S. F. Martina-Perez, I. B. Breinyn, D. J. Cohen, R. E. Baker, Optimal control of collective electrotaxis in epithelial monolayers. *Bull. Math. Biol.* **86**, 95 (2024).
58. B. A. Camley, W. J. Rappel, Cell-to-cell variation sets a tissue-rheology-dependent bound on collective gradient sensing. *Proc. Natl. Acad. Sci. U.S.A.* **114**, e10074–e10082 (2017).
59. F. Durant *et al.*, The role of early bioelectric signals in the regeneration of planarian anterior/posterior polarity. *Biophys. J.* **116**, 948–961 (2019).
60. X. Trepat *et al.*, Physical forces during collective cell migration. *Nat. Phys.* **5**, 426–430 (2009).
61. G. Tai, B. Reid, L. Cao, M. Zhao, Electrotaxis and wound healing: Experimental methods to study electric fields as a directional signal for cell migration. *Methods Mol. Biol.* **571**, 77–97 (2009).
62. Z. Pincus, J. A. Theriot, Comparison of quantitative methods for cell-shape analysis. *J. Microsc.* **227**, 140–156 (2007).
63. E. L. Barnhart, K. C. Lee, K. Keren, A. Mogilner, J. A. Theriot, An adhesion-dependent switch between mechanisms that determine motile cell shape. *PLoS Biol.* **9**, e1001059 (2011).
64. K. Keren *et al.*, Mechanism of shape determination in motile cells. *Nature* **453**, 475–480 (2008).
65. F. Graner, J. A. Glazier, Simulation of biological cell sorting using a two-dimensional extended Potts model. *Phys. Rev. Lett.* **69**, 2013–2016 (1992).
66. M. H. Swat *et al.*, Multi-scale modeling of tissues using CompuCell 3D. *Methods Cell Biol.* **110**, 325–366 (2012).
67. T. E. Angelini, E. Hannezo, X. Trepat, J. J. Fredberg, D. A. Weitz, Cell migration driven by cooperative substrate deformation patterns. *Phys. Rev. Lett.* **104**, 168104 (2010).
68. S. R. Vedula *et al.*, Emerging modes of collective cell migration induced by geometrical constraints. *Proc. Natl. Acad. Sci. U.S.A.* **109**, 12974–12979 (2012).
69. A. Szabó *et al.*, In vivo confinement promotes collective migration of neural crest cells. *J. Cell Biol.* **213**, 543–555 (2016).
70. J. Varennes, B. Han, A. Mugler, Collective chemotaxis through noisy multicellular gradient sensing. *Biophys. J.* **111**, 640–649 (2016).
71. C. Copos, CoposGroup/Galvanotaxis. GitHub. https://github.com/CoposGroup/Galvanotaxis. Accessed 5 May 2025.

Supplemental Materials include:

Supplemental Figure Legends
Movie Legends
Five Supplemental Figures
Modeling Supplement

SUPPPLEMENTAL FIGURE LEGENDS

SUPPLEMENTAL FIGURE 1: Voltage dependency of fish keratocyte group migration in the absence and presence of PI3K inhibitor.
A. Box plots showing voltage-dependent directional migration under control (Ctrl) conditions, assessed by directedness (left) and trajectory speed (right) across different EF strengths (0, 0.5, 1, 2, and 4 V/cm). Directedness is significantly biased toward the cathode in both small (S, ≤75 cells) and large (L, >75 cells) groups from 1 to 4 V/cm compared to 0–0.5 V/cm. Trajectory speed increases with EF strength and peaks at 2–4 V/cm.**, $p < 0.01$, unpaired two-tailed *t*-test on combined samples.
B. Box plots showing directedness (left) and trajectory speed (right) under PI3K inhibition (LY). Significant differences are observed between small (S, ≤35 cells) and large (L, >35 cells) groups at 1–4 V/cm, with some of the small groups beginning to bias toward the anode. As in control conditions, speed peaks at 2–4 V/cm.**, $p < 0.01$, unpaired two-tailed *t*-test on combined samples. Based on these results, 1–2 V/cm was selected for subsequent experiments.

SUPPLEMENTAL FIGURE 2: PI3K inhibition-induced EF-directed reversal is size-dependent.
Box plots showing the sizes of fish keratocyte groups migrating toward the anode (red), with no directional bias (orange), or toward the cathode (blue) under LY treatment. Only small groups exhibited biased migration toward the anode, while both small and large groups could migrate toward the cathode or remain unbiased. $p < 0.01$ by unpaired two-tailed student *t*-test.

SUPPLEMENTAL FIGURE 3: PI3K inhibition induces EF-directed reversal of group migration toward the anode in a dose-dependent manner.
Stacked bar plots showing the percentage of fish keratocyte groups (ranging from 2 to 400 cells) migrating toward the cathode (blue), anode (red), or displaying no directional bias (gray) under increasing concentrations of LY294002 (0–200 μM). An increasing proportion of groups reverse direction and migrate toward the anode with higher LY concentrations. $p = 0.011$ by Chi-square (χ^2) test.

SUPPLEMENTAL FIGURE 4: EF-guided collective cell migration of fish keratocytes.
A. Schematic view of the electrotaxis chamber and the setup for EF application.
B. Workflow for image processing. Cell group movement was monitored by overlapped multi-field time lapse recording. Multi-field images were stitched together as described in Methods and assembled into temporally ordered stacks for subsequent quantification.
C. Cell numbers in groups was either counted directly or estimated per squared unit area. Scale bar: 50 μm.
D. Groups were outlined and their movements before and after EF application were tracked manually or automatically in ImageJ. Morphological changes were characterized by shape analysis.

SUPPLEMENTAL FIGURE 5: Lamellipodia at the front and rear of large cell groups.
(A) Phase contrast images of a large keratocyte group at the onset (0 min) and after 15 and 30 minutes of EF application in the indicated orientation (Ctrl). Insets show magnifications of the highlighted

cathodal/anodal edge areas, showing intact lamellipodia (dashed enclosures). This group contains approximately 54 cells. Scale bar, 100 µm. Time stamps in mm:ss.
(B) Phase contrast images of a large keratocyte group at the onset (0 min) and after 15 and 30 minutes of EF application in the indicated orientation, in the presence of a PI3K inhibitor (LY). Insets show magnifications of the highlighted cathodal/anodal edge areas, showing intact lamellipodia after EF application (dashed enclosures). This group contains approximately 52 cells. Scale bar, 100 µm. Time stamps in mm:ss.

MOVIE LEGENDS

Movie 1: Pair of PI3K-inhibited cells without and with EF.

Movie 2: Three small groups of unperturbed cells polarizing and initiating collective migration in EF.

Movie 3: Four small groups of PI3K-inhibited cells polarizing and initiating collective migration in EF.

Movie 4: Large group of unperturbed cells polarizing and initiating collective migration in EF.

Movie 5: Large group of PI3K-inhibited cells polarizing and initiating collective migration in EF.

Movie 6: 2D simulations of small and large groups of unperturbed and PI3K-inhibited cells polarizing and initiating collective migration in EF.

Movie 7: 2D simulations of the dumbbell-shaped group of PI3K-inhibited cells polarizing and initiating collective migration in EF.

Movie 8: Experimentally observed dumbbell-shaped group of PI3K-inhibited cells polarizing and initiating collective migration in EF.

Movie 9: Experimentally observed elongated group of PI3K-inhibited cells polarizing in EF, with small daughter groups splitting from the mother group and initiating motility in the opposite direction.

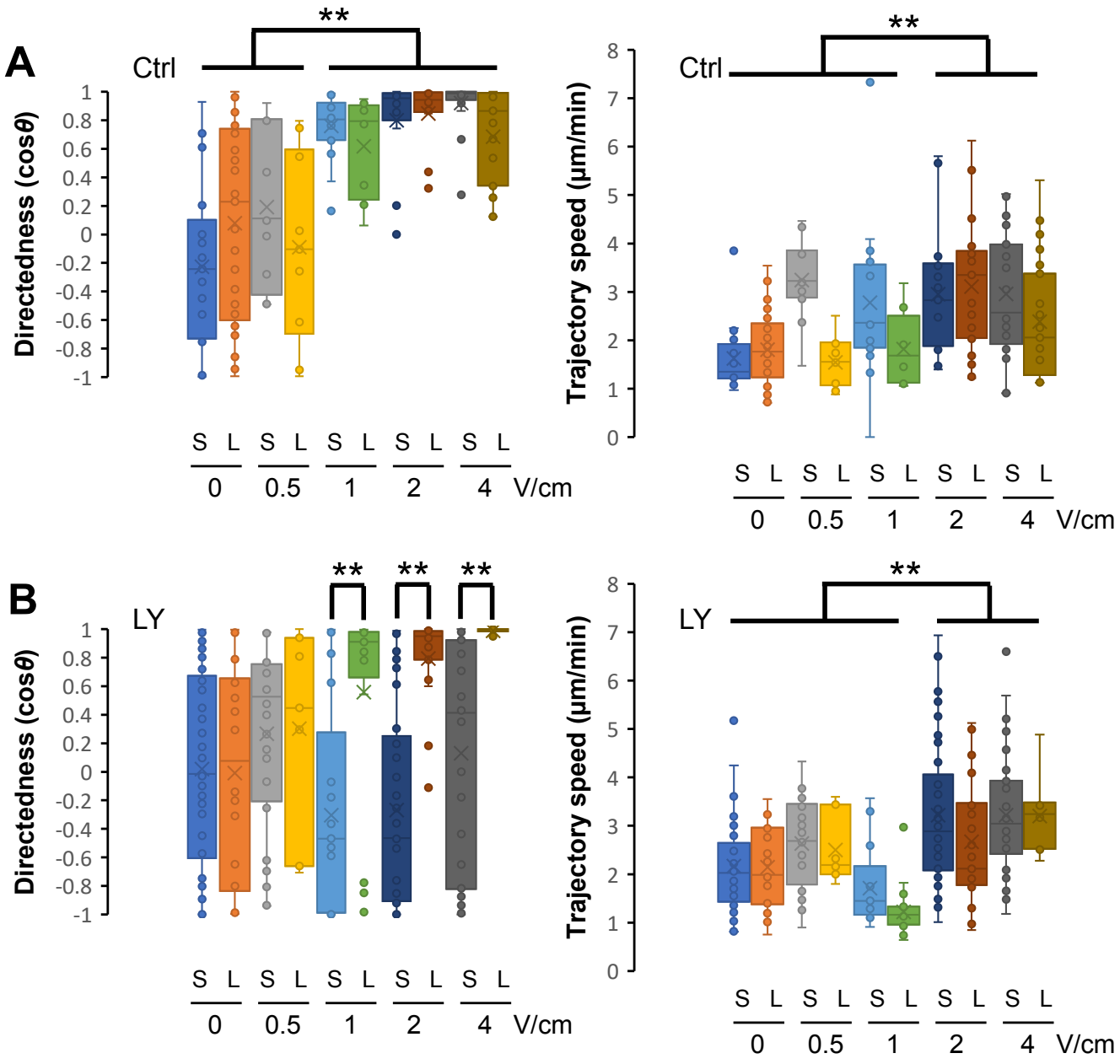
A
Ctrl
**
Directedness (cosθ)
1
0.8
0.6
0.4
0.2
0
-0.2
-0.4
-0.6
-0.8
-1
S L S L S L S L S L
0 0.5 1 2 4 V/cm
Trajectory speed (μm/min)
8
7
6
5
4
3
2
1
0
B
LY
**
**
**

Fig S1

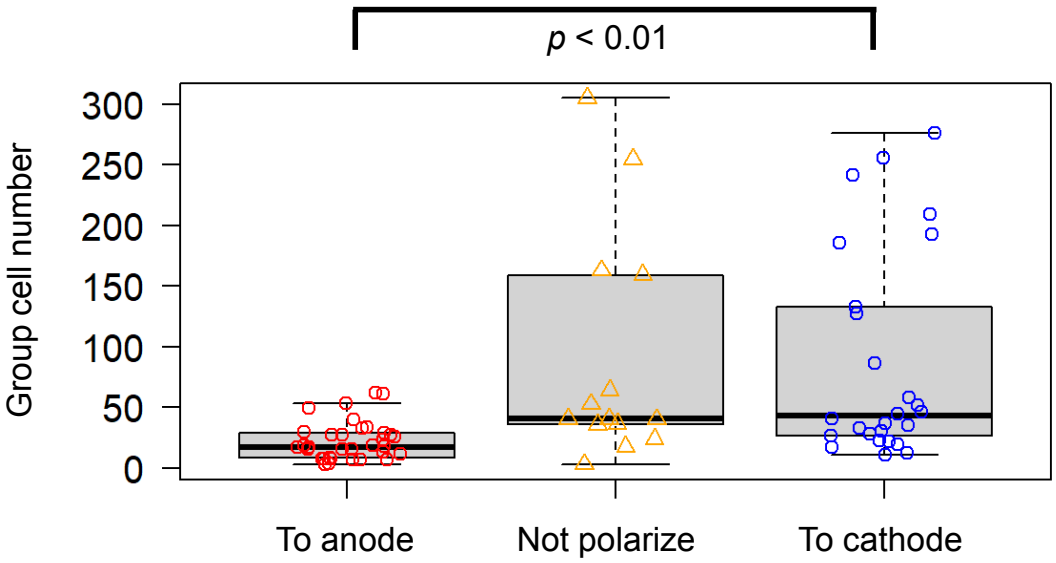
p < 0.01
Group cell number
300
250
200
150
100
50
0
To anode
Not polarize
To cathode

Fig S2

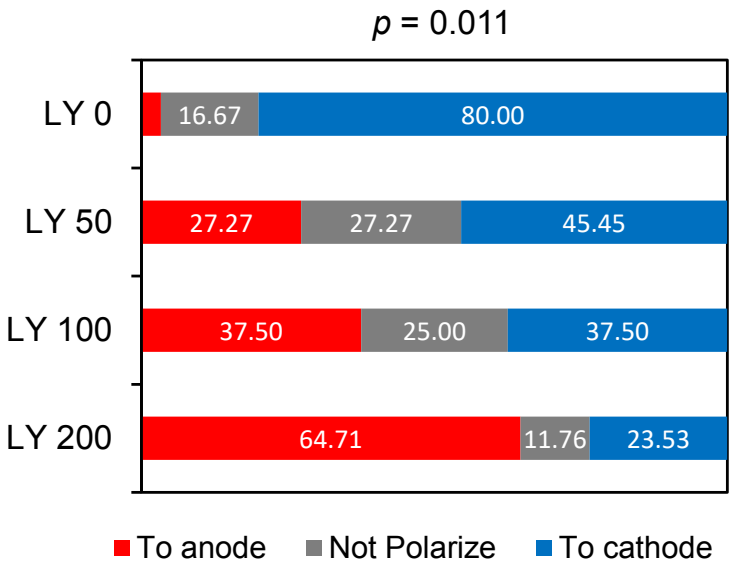
p = 0.011
LY 0
LY 50
LY 100
LY 200
16.67
80.00
27.27
27.27
45.45
37.50
25.00
37.50
64.71
11.76
23.53
To anode
Not Polarize
To cathode

Fig S3

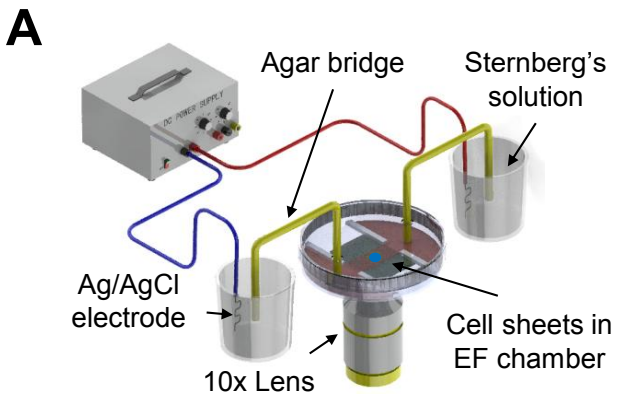

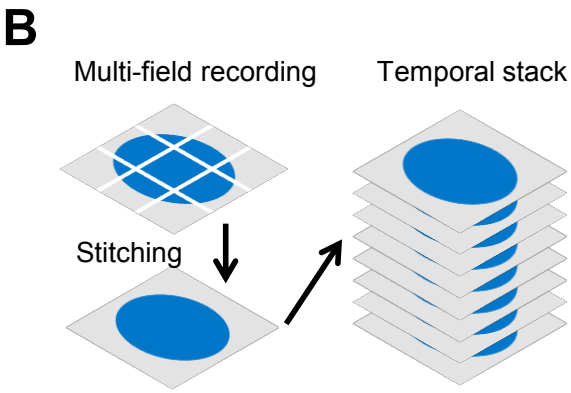

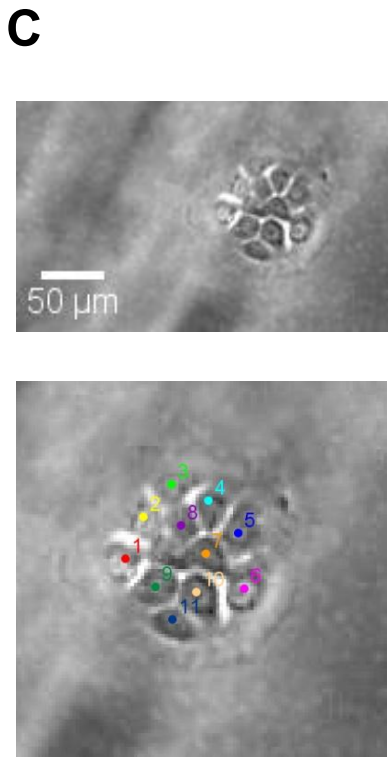

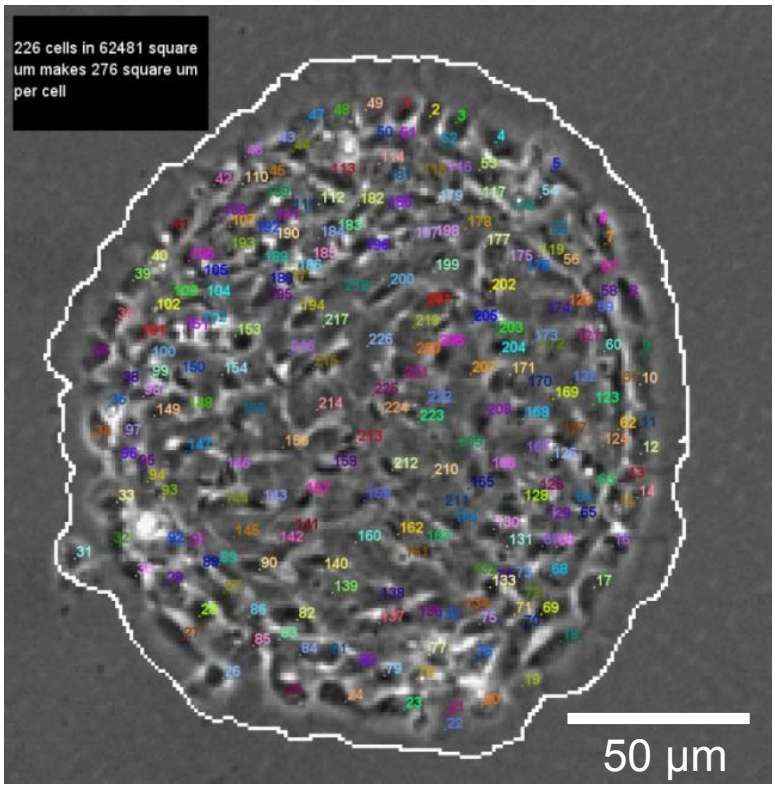

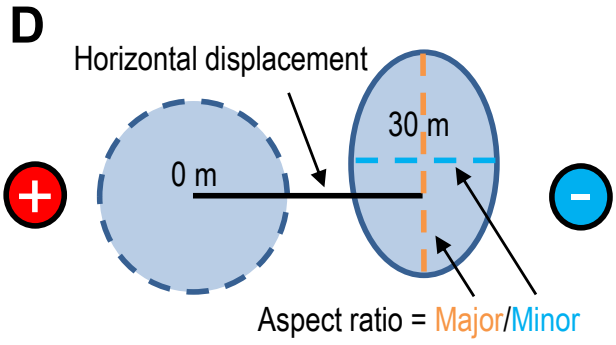

N. Horizontal displacement = X $D_{30\ m\ after\ EF} - X\ D_{0\ m\ before\ EF}$

N. AR change = $(AR_{30\ m\ after\ EF} - AR_{0\ m\ before\ EF})/AR_{0\ m\ before\ EF}$

N. Area change = $(Area_{30\ m\ after\ EF} - Area_{0\ m\ before\ EF})/Area_{0\ m\ before\ EF}$

Fig S4

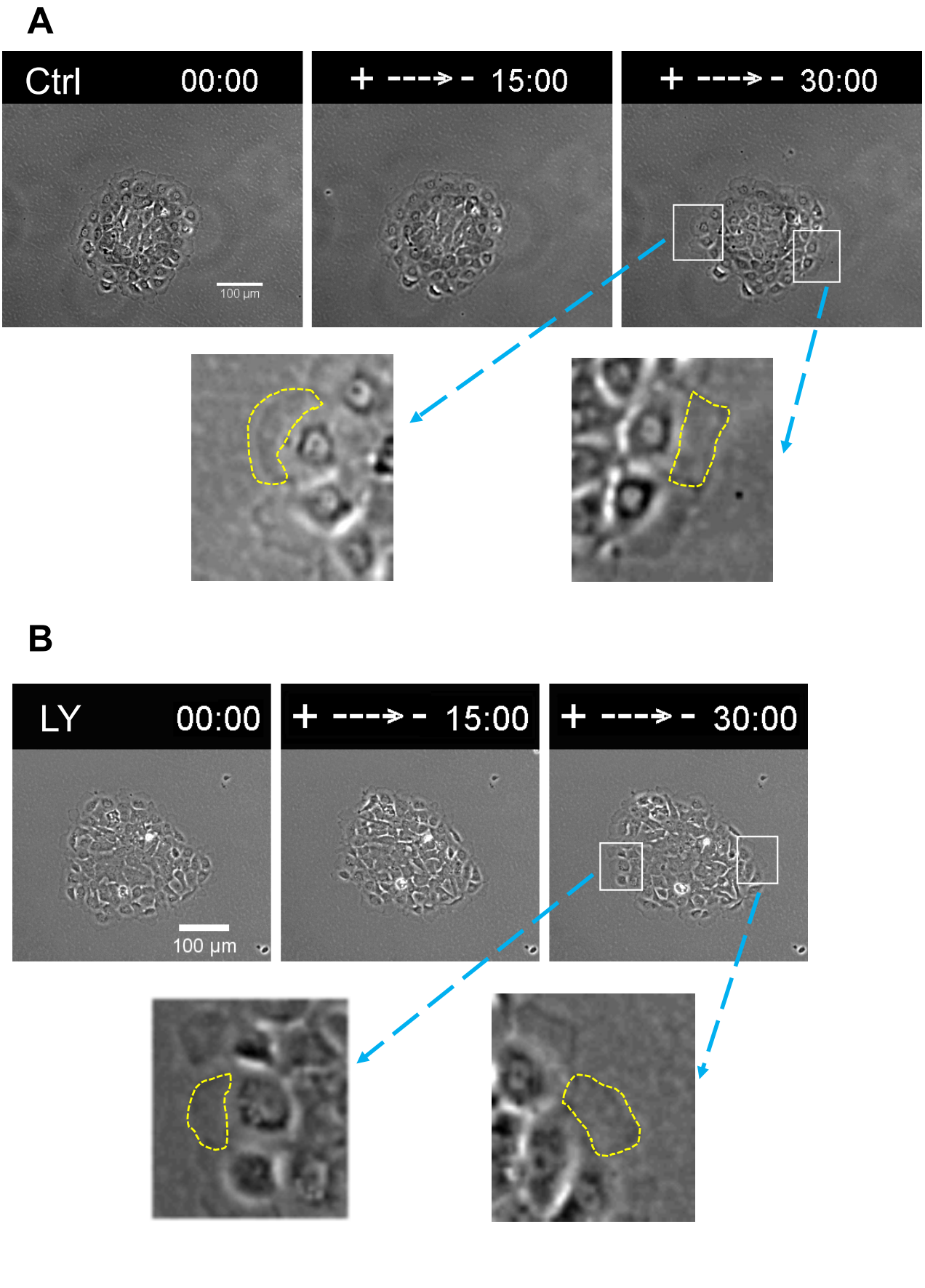

Fig S5

Galvanotactic directionality of cell groups depends on group size: Modeling Supplement

Supplemental Material

Calina Copos Yao-Hui Sun Kan Zhu Yan Zhang Brian Reid
Bruce Draper Francis Lin Haicen Yue Yelena Bernadskaya Min Zhao
Alex Mogilner

A. Qualitative model description

To probe the interactions that would give rise to the observed movement of cells of different group sizes in the presence of electric field (EF) application, we introduce a computational model. In our model, each biological cell is represented by its position $\vec{x} = (x, y)$ in a two-dimensional spatial domain, and it generates a propulsive force dependent on EF application, locally interacts with its neighboring cells and the substrate underneath (Fig. 3A). Cells move according to their local force balance as well as mechanical noise:

$$\vec{F} - \zeta \frac{d\vec{x}}{dt} + \eta \mathcal{N}(0, 1) = 0, \tag{S1}$$

since cells are not subject to inertial forces due to the very low Reynolds number [1, 2]. $\mathcal{N}(0, 1)$ denotes a Gaussian random variable of mean zero and unit variance, sampled independently for each cell and at each time step. The substrate applies effective viscous passive drag (friction) forces to moving cells, $\zeta d\vec{x}/dt$ where $d\vec{x}/dt$ is the cell velocity and ζ is the viscous drag coefficient. Each cell generates and applies: (1) outward propulsive forces due to the migratory nature of keratocytes ($\vec{F}_{\text{outward}}$), (2) EF-induced propulsive forces along the EF vector ($\vec{F}_{\text{propulsive}}$), and (3) intercellular forces due to cell-cell interactions ($\vec{F}_{\text{cc}}$), such that

$$\vec{F} = \vec{F}_{\text{outward}} + \vec{F}_{\text{propulsive}} + \vec{F}_{\text{cc}}. \tag{S2}$$

Intercellular and outward forces: The intercellular forces are modeled through passive elastic springs connecting any two neighboring cells with nonzero rest length (ℓ_0) and spring stiffness (k) (inset, Fig. 3A). The outward forces are only applied to edge (outer) cells, and these forces have magnitude $|\vec{F}_{\text{outward}}| = f_{\text{p}}$ and point in the outward normal direction.

Propulsive EF-induced forces: The model assumes that cells within a group sense the application of an EF individually and independently [3, 4]. The magnitude and directionality of the EF-induced propulsive forces depend on the cell position in the group (outer or inner cell) and on the cell chemical state (unperturbed or PI3K-inhibited). We discuss the various scenarios below:

- No EF: In the absence of EFs, inner cells do not generate propulsive forces.

- Unperturbed (Ctrl) cell group: With EF application, inner cells generate propulsive forces of magnitude f_i towards the cathode. Outer cells lamellipodia of which are on the cathodal side generate propulsive forces of magnitude F_0 towards the cathode, while outer cells on the anodal side generate forces of magnitude $F_1 < F_0$ in the anodal direction (Ctrl inset, Fig. 3A).

$$\vec{F}_{\text{propulsive}} = \begin{cases} f_i\,\widehat{x} & \text{for inner cells,} \\ F_0\,\widehat{x} & \text{for edge cells on the cathode side,} \\ -F_1\,\widehat{x} & \text{for edge cells on the anode side,} \end{cases}$$

  where $\widehat{x}$ is a unit vector pointing in the x-direction.

- PI3K-inhibited (LY) cell group: Similar to the unperturbed cell group, in the presence of the EF, inner cells generate propulsive forces of magnitude f_i in the cathodal direction. Outer cells facing the cathode generate propulsive forces of magnitude $F_1 < F_0$ in the cathodal direction, while outer cells on the anodal side produce propulsive forces of magnitude F_0 in the anodal direction (LY inset, Fig. 3A).

$$\vec{F}_{\text{propulsive}} = \begin{cases} f_i\,\widehat{x} & \text{for inner cells} \\ F_1\,\widehat{x} & \text{for edge cells on the cathode side,} \\ -F_0\,\widehat{x} & \text{for edge cells on the anode side.} \end{cases}$$

Morphological changes: To implement the group shape changes observed in small clusters, we set a velocity-based threshold for the propulsive forces of outer cells. Namely, outer cells engage their lamellipodia and generate propulsive forces only if their velocity is above $(-v_{\text{EF}})$. If an edge cell's speed is lower than $(-v_{\text{EF}})$, its lamellipodia is lost and propulsive forces are zero. The value for v_{EF} is chosen so that groups larger than ~ 60 cells are engaged (i.e. all edge cells generate propulsive forces) and its numeric value is provided in Table S1. The stability condition for maintaining propulsive forces changes in PI3K-inhibited groups – a cathode facing outer cell will generate nonzero propulsive force if its velocity is above than $(-v_{\text{LY}})$.To capture the changes in aspect ratio and area of small groups, we further introduced a couple of dynamics that do not qualitatively impact the group's velocity. Once an outer cell disengages (i.e. its propulsive force becomes zero as described above) two changes are implemented: (1) the elastic springs connected to the disengaged edge cell are set to have nearly zero rest length, (2) the drag coefficient of disengaged edge cells is decreased by a factor of 10.

Non-dimensional model parameters are listed in Table S1 and the computational results are summarized in Table S2 and Fig. 3. To produce the results displaying variability close to the data, we introduced variability that stems from two sources: number of cells in groups and magnitude of propulsive forces. The simulations were done for small groups of 16 and 30 cells, and for large groups of 128 and 252 cells. Plus, for each simulation, the magnitude of the propulsive force was picked from a uniform distribution with mean value as shown in Table S2 and a 10% standard deviation. Below, we discuss numerical implementation details along with rationale for parameter choices.

B. Numerical implementation

Initialization: Given a disk domain shape, the domain is coarse-grained using the distmesh package [5] which employs Delaunay triangulation to generate a network of points with links of equal

length. The cell positions are chosen to be the vertices of the triangulation, and the elastic springs between cells to its nearest neighbors lie on the edges of the triangulation. All springs are created in an undeformed state, such that initially the network has no passive internal stresses, and if no external or propulsive forces are applied then the material does not deform. The starting configuration is a uniformly stretched cluster (by 10%).

Time-stepping: The force balance can be re-written as an equation of motion:

$$\frac{d\vec{x}}{dt} = \frac{1}{\zeta}\left(\vec{F}_{\text{outward}} + \vec{F}_{\text{propulsive}} + \vec{F}_{\text{cc}} + \eta\mathcal{N}(0,1)\right). \tag{S3}$$

Given the initial positions, forces are computed for every cell within the cluster according to the description in the previous section. We use Forward Euler finite difference method for temporal discretization of the equation of motion in Eq. S3. The time step is chosen to meet numerical stability constraints.

C. Justification of model parameters

Next, we discuss the motivation for the choice of parameters in Table S1 and the impact on the model results with changes in parameters. The group movement dynamics are primarily governed by 5 parameters: the magnitude of the propulsive forces of inner and outer cells: f_i, F_0, F_1 and their corresponding drag coefficients: ζ_i and ζ_e. There are multiple sets of parameters that reproduce the following experimental observation: in the presence of EF, both unperturbed (Ctrl) and PI3K-inhibited (LY) large groups move slowly to the cathode, while small Ctrl groups move faster than larger groups to the cathode, but small LY groups move to the anode.

To illustrate how model parameters are chosen to capture this key experimental observation, we consider a 1D simplified scenario (Fig. 1H) in the limit of high elastic stiffness and the absence of protrusive outward forces or mechanical noise. The equation of motion in Eq. S3 becomes

$$(2\zeta_e + N\zeta_i)\, v = F_{\text{propulsive}}. \tag{S4}$$

In this scenario, there are N inner cells which are bounded on either side by one edge cell. The group velocity for unperturbed groups in the presence of EF application is

$$v_1(N) = \frac{F_0 - F_1 + Nf_i}{2\zeta_e + N\zeta_i}. \tag{S5}$$

To capture the observation that larger groups move slower than smaller groups, we require the group velocity to be a decreasing function with the group size (blue curve, Fig. MS1). Mathematically, this implies the following second constraint on the parameters:

$$v_1'(N) < 0 \Rightarrow 2f_i\zeta_e + \zeta_i(F_1 - F_0) < 0. \tag{S6}$$

In the limit of no inner cells, Eq. S5 yields an upper limit

$$\lim_{N\to 0} v_1(N) = v_0 = \frac{F_0 - F_1}{2\zeta_e},$$

while in the limit of an infinitely large group, Eq. S5 provides a lower limit

$$\lim_{N\to\infty} v_1(N) = v_\infty = \frac{f_i}{\zeta_i}.$$

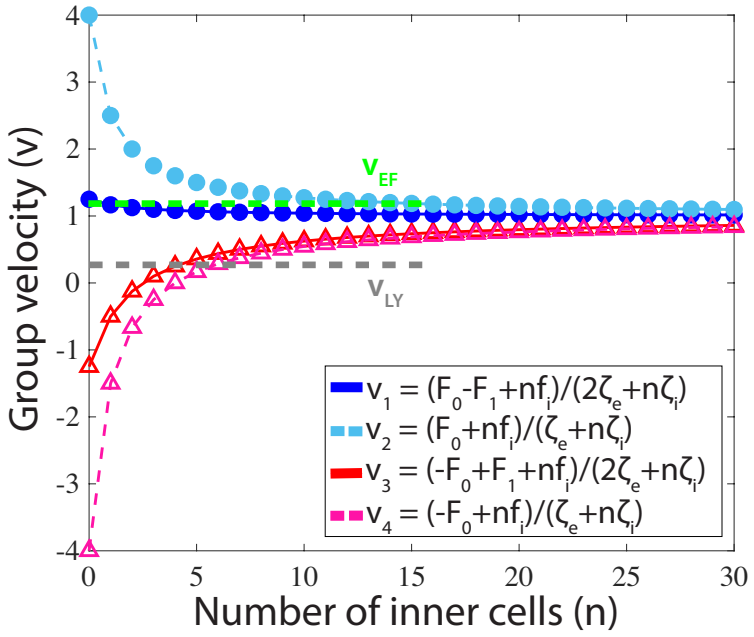

Figure MS1: Results of the 1D model. For the given parameters, group velocity v is shown as a function of the number of inner cells n along a one-dimensional configuration in the presence of an EF. v_1 denotes the uninhibited group velocity when both edge and inner cells exert propulsive forces, while v_3 is the same condition but for PI3K-inhibited groups. v_2 is the velocity when only the right (cathode-facing) edge cell and inner cells produce propulsive forces, and v_4 is the asymmetric velocity for PI3K-inhibited groups. The rupture force of edge cells in uninhibited groups is v_{EF} (green dashed line) and it is v_{LY} (gray dashed line) for PI3K-inhibited groups.

To constrain the parameter space, we seek to match the observation that small groups move 1.5–3× faster than large groups and, thus

$$v_0 \approx 1.5\text{–}3 \times v_\infty. \tag{S7}$$

Even with the above constraints, there are an infinite number of parameter combinations. In PI3K-inhibited groups, the edge cell facing the cathode generates a propulsive force $F_1 < F_0$ in the x-direction; similarly, the edge cell away from the cathode produces a propulsive force F_0 in the negative x-direction. The group velocity for N inner cells bounded on either side by one edge cell from Eq. S4 becomes

$$v_3(N) = \frac{F_1 - F_0 + N f_i}{2\zeta_e + N\zeta_i}.$$

From the experiments, we know that the critical group size separating large from small groups is around 35 cells. This gives us a constraint on the system for the speed to change signs depending on the number of inner cells. Specifically, we require that groups larger than 35 cells, which corresponds to $N \approx 3-4$ inner cells along a horizontal line, move toward the cathode

$$v_3(N) > 0 \Rightarrow F_1 - F_0 + N f_i > 0, \tag{S8}$$

for $N > 3$ (red curve, Fig. MS1). One (but not unique) set of parameters that meet the above conditions, namely Eqs. S6, S7 and S8, are $f_i = 0.5$, $F_0 = 2.0$, $F_1 = 0.75$, and $\zeta_i = \zeta_e = 0.5$.

Parameter	Description	Numeric value
ζ_i	Viscous drag coefficient of inner cells	0.5
ζ_e	Viscous drag coefficient of edge cells	0.5
k	Elastic spring stiffness constant	2.0
ℓ_0	Resting spring length	0.35
f_i	Magnitude of propulsive forces for inner cells	0.5
F_0	Magnitude of propulsive forces for edge cells	2.0
F_1	Magnitude of propulsive forces for edge cells	0.75
f_p	Magnitude of outward contribution of pull forces for edge cells	4.0
v_thr	Threshold breakage velocity for edge cells (without EF)	4.0
$v_\mathrm{EF}, v_\mathrm{LY}$	Rupture breakage velocity for edge cells (with EF)	1.2 (Ctrl), 0.2 (LY)
η	Random noise coefficient	1.0
Δt	Time step	0.00001

Table S1: Simulation non-dimensional parameters.

To find the threshold breakage velocity, v_thr, we consider the stability of the scenario where no external EF is applied. In this case, inner cells do not generate propulsive forces, but outer cells do generate propulsive force F_0 in the outward direction. The resulting group speed is $v = \frac{F_0}{2\zeta_e + N\zeta_i}$. For a group with any number of inner cells to be stable, we need $v_\mathrm{thr} > F_0/(2\zeta_e)$. The constraint sets the threshold breakage velocity, meaning an outer cell will generate a propulsive force if its velocity is higher than $(-v_\mathrm{thr})$. If the velocity is lower than $(-v_\mathrm{thr})$, the propulsive forces are zero.

Next, we need to set the rupture velocity, v_EF, with an external EF. The choice of this parameter essentially sets the difference from large, symmetric to small, asymmetric groups. In uninhibited groups, we want the stability of the anode-facing edge cells to be lost – an anode-facing cell generates propulsive force F_1 if its speed is higher than $-v_\mathrm{EF} < v_\mathrm{break}$ and zero propulsive force otherwise (green line, Fig. MS1). In PI3K-inhibited groups, the same condition is set but for the cathode-facing cells with rupture velocity $v_\mathrm{LY} < v_\mathrm{EF}$ (gray line, Fig. MS1).

With no impact to the overall dynamics, a mechanical noise is introduced with the same order of magnitude as the elastic forces. Again, with no impact on the overall dynamics, a radially outward force is added for edge cells in groups of all sizes with magnitude f_p. The reasoning for this is to match the aspect ratio change more closely in small versus large groups. The spring stiffness, $k = 2.0$, was chosen to match the observation that the change in aspect ratio of large groups is small (approximately, 0.1). Increasing spring stiffness results in a smaller change in aspect ratio, while decreasing spring stiffness results in a larger change in aspect ratio and for small enough spring stiffness, a positive area change.

D. Comparison with experimental data & parameter variations

The model reproduces key qualitative observations: large groups move slower than the small ones; unperturbed groups move faster than PI3K-inhibited groups of the same size; aspect ratios and areas of the small groups change more than those of the large groups (Table S2, Fig. MS2). The order of magnitude of the aspect ratios and area changes and of the relative group displacements are also similar to respective data (compare Fig. MS2 and Fig. 1G and Fig. 2I). However, there are also some notable differences between the numerical results and the experimental findings. First, in the simulations, large groups move disproportionally slower than small groups compared with the data. For example, experimental findings report that, on average, PI3K-inhibited small groups

migrate at roughly half the speed of uninhibited large groups. In our model, we find that difference to be closer to a factor of 1/7 rather than 1/2. However, we are limited by the model constraints and cannot find a closer match to experimental values. Specifically, to find a closer match to the trend that larger groups move at similar, but slower, speeds to small groups we would like to either increase the inner propulsive forces, f_i, or decrease the edge cathode-facing propulsive forces, F_0. Either one of the variations would result in loss of the constraint that velocity is a decreasing function of the inner cell number in Eq. S6. This would result in a "flat" blue curve in Fig. MS1 which would make it impossible to set a threshold breakage velocity to separate small from large groups. Attempting to decrease the anode-facing edge propulsive force, F_1, has a similar effect. Lastly, decreasing the viscous drag coefficient results in a larger discrepancy in speed between small and large cell groups, while increasing the drag coefficient results in a loss of the constraint that group velocity is a decreasing function of the inner cell number. This said, note that there is a great variability in the experimental data, and there are certain large and small groups, displacements and area and aspect ratio changes of which are reproduced by the model very well. Ultimately, it is likely that a number of complex factors, including, but not limited to, cell to cell variability in propulsive forces and drags, supracellular effects on group edges and delicate position-dependent variations of parameters inside the groups are necessary for the model to reproduce the data with high precision.

Group size	**No EF**	**Ctrl**			**LY**		
	v	Δx	ΔA	ΔAR	Δx	ΔAR	ΔA
Small (16, 30 cells)	$-5.81e{-5}$ $\pm 3.1e{-4}$	8.53 ± 1.87	-0.57 ± 0.01	0.18 ± 0.01	-5.81 ± 2.44	-0.56 ± 0.02	0.15 ± 0.01
Large (128, 252 cells)	$-1.04e{-5}$ $\pm 4.9e{-5}$	2.59 ± 0.15	-0.09 ± 0.01	0.12 ± 0.01	1.14 ± 0.22	-0.09 ± 0.01	0.12 ± 0.01

Table S2: Resulting mean and $\pm$ standard deviation for the group speed and morphological measurements, area and aspect ratio, from simulations with parameters as indicated in Table S1. v denotes velocity in arbitrary units, Δx denotes displacement, ΔAR denotes change in aspect ratio from the initial configuration aspect ratio (i.e. 1), and ΔA is the change in area from the initial configuration.

E. Results for nonlinear elastic cell-cell adhesions

The rationale for modeling cell-cell adhesions as linear spring-like forces is to keep the model simple and only introduce additional assumptions which are needed to capture experimental observations. Moreover, our observations suggest that no more than 3% of the cells exchange neighbors, which further justifies effectively elastic, spring-like adhesions between the cells. However, the separation of PI3K-inhibited bilobed-shaped clusters into two separate lobes does pose an interesting question – what would the response of the model be with rupture of cell-cell adhesions above a threshold load force – essentially, a slip-like response [6]? To answer this, a slip response was implemented with a piecewise constant stiffness, k, that is zero if the cell-cell force exceeds a threshold load and nonzero otherwise. We find that PI3K-inhibited dumbbell-shaped clusters indeed do separate into two or three subgroups depending on the threshold load (Fig. MS3). Initially, the larger lobe wins

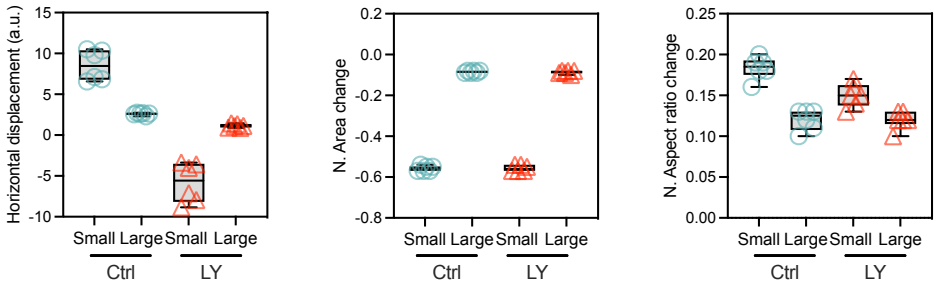

Figure MS2: Summary of simulation results. (A) Horizontal displacement after EF application in large and small cell groups in the absence (Ctrl) and presence (LY) of the PI3K inhibitor. (B-C) Normalized area change and aspect ratio from initial configuration right before EF application.

the tug-of-war and drags the whole cluster towards the cathode, but eventually the smaller lobe, below critical size, separates from the cathode-moving cluster and migrates towards the anode, opposite of the larger cluster.

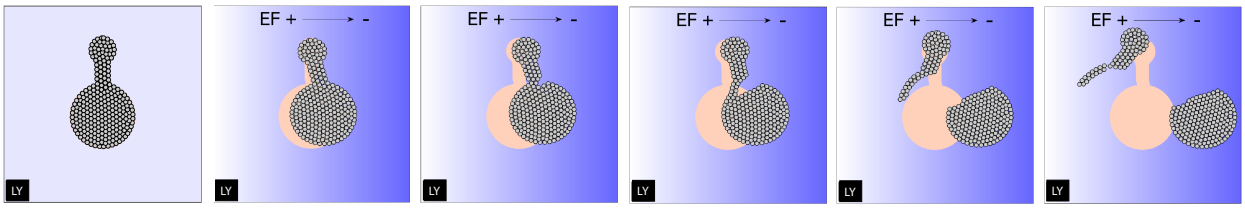

Figure MS3: Nonlinear slip-like response of cell-cell adhesions in 2D model produces breakage of PI3K-inhibited bilobed-shaped cluster. If a rupture load is introduced in the spring-like cell-cell adhesion model, the PI3K-inhibited bilobed-shaped clusters can separate into subgroups depending on the threshold load. Initially, the larger lobe wins the tug-of-war and drags the whole cluster towards the cathode, but eventually the smaller lobe, below critical size, separates from the cathode-moving cluster and migrates towards the anode, opposite of the larger cluster.

Notably, if the same setup is used for PI3K-inhibited disk-shaped clusters this also results in separation into two similarly-sized lobes. As this finding is not supported experimentally, we set the value of the threshold load to ensure PI3K-inhibited disk-shaped clusters do not separate, and lower the elastic stiffness in the cell-cell adhesion of dumbbell-shaped clusters to obtain the separated lobes in Fig. MS3. The reason for the similar response in biloped- and disk-shaped clusters is simple – rupture depends on the stretch of cell-cell links (equivalently, threshold load), but the same stretch also underpins the shape deformations of disk-shaped groups reported experimentally. Thus, there is a careful balance between both allowing shape deformations and rupture. When Maxwell viscoelastic springs (i.e. elastic and dashpot elements connected in series) were implemented instead of elastic spring-like interactions, we found that the nonlinear response did not affect our findings – namely, the viscoelastic response of cell-cell links did not allow us to use the same parameters in disk and dumbbell-shaped curves to obtain conditional rupture in only one group. A future investigation into rupture of cell clusters into smaller groups is necessary and our preliminary results indicate it oought to include more sophisticated intercellular adhesions.

Supplemetary References

[1] Vignaud, T. et al. (2021) *Stress fibres are embedded in a contractile cortical network*. Nat Mat, 20:410-420, doi: 10.1038/s41563-020-00862-8

[2] Alert, R. and Trepat, X. (2020) *Physical models of collective cell migration*. Ann Rev Cond Mat Phys, 11:77-101, doi: 10.1146/annurev-conmatphys-031218-013516.

[3] Sun, Y. et al. (2023) *EF–guided collective motility initiation of large epidermal cell groups*. Mol Biol Cell 34:ar48, doi: 10.1091/mbc.E22-09-0391.

[4] Sun Y. et al. (2013) *Keratocyte fragments and cells utilize competing pathways to move in opposite directions in an EF*. Curr. Biol. 23:569–574, doi: 10.1016/j.cub.2013.02.026.

[5] Persson P.-O. and Strang, G. (2004) *A simple mesh generator in MATLAB*. SIAM Rev. 46:329-345, doi: 10.1137/S0036144503429121.

[6] Bell, G. I. (1978) *Models for the specific adhesion of cells to cells* Sci. 200: 618-627, doi: 10.1126/science.347575